Icarus 390 (2023) 115322

Contents lists available at ScienceDirect

Icarus

journal homepage: www.elsevier.com/locate/icarus

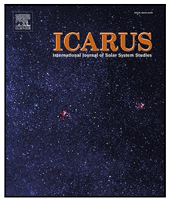

Research Paper

The heterogeneous response of martian meteorite Allan Hills 84001 to planar shock

Thomas L. North [a,*], Gareth S. Collins [a], Thomas M. Davison [a], Adrian R. Muxworthy [a], Sarah C. Steele [b], Roger R. Fu [b]

[a] Imperial College London, Department of Earth Science and Engineering, London, SW7 2AZ, UK
[b] Harvard University, Department of Earth and Planetary Sciences, Cambridge, 02138, MA, USA

ARTICLE INFO

Keywords:
Mars
Meteorites
Impact processes

ABSTRACT

Impact-generated shock waves can change the physical properties of meteorites and their constituent minerals. Accounting for these effects is key to recovering information about the early solar system from meteorite observations. ALH 84001 is a rare ancient sample from the Martian crust, providing a unique window into the thermal and metamorphic evolution of Mars. A well-studied meteorite, past geochemical and petrologic investigations have attempted to deduce its thermal and impact history with some contradictory results. By simulating the passage of a planar shock wave through a synthetic analog for samples of ALH 84001 using the iSALE-2D shock physics code we have determined the meteorite's likely thermodynamic and physical response during an impact. Our simulations show that heterogeneous shear heating, induced by the planar shock wave, can produce strong thermal gradients on the sub-millimeter 'mesoscale' throughout the meteorite, even in relatively weak shock waves (< 5 GPa). We are able to place new constraints on deformation events experienced by the meteorite during its time on the parent body, including the maximum pressure ALH 84001 has experienced since it acquired its remanent magnetization and its subsequent ejection from Mars.

1. Introduction

Intense shock waves generated by impacts on planetary surfaces are understood to be significant drivers of metamorphic and environmental evolution on a planet-wide scale. Impacts on Earth have led to mass extinctions and the beginning of ice ages (Schulte et al., 2010; Schmitz et al., 2019). While terrestrial impact sites are typically characterized following an investigation into the subsurface structure of a crater site, impacts on other planets can be characterized from either Earth-based observation or inspection of physical samples that have been collected in the form of meteorites. Meteorites in particular store a unique record of the surface and interior evolution of planetary bodies.

Martian meteorite Allan Hills 84001 (ALH 84001) was recovered from Antarctica in 1984 and became a highly prominent sample following the discovery of what was argued to be biogenic magnetite (McKay et al., 1996; Thomas-Keprta et al., 2000, 2001). While subsequent studies suggested an abiotic origin more likely for all minerals present in the meteorite (Brearley, 2003; Golden et al., 2004; Fortin and Langley, 2005; Steele et al., 2007), ALH 84001 remains of great interest as it hosts a unique record of the evolution of Mars, providing a window to further our understanding of the metamorphic, petrologic and paleomagnetic history of the planet (Kirschvink et al., 1997; Treiman, 1998; Hartmann and Neukum, 2001).

ALH 84001 is an orthopyroxenite meteorite containing coarse-grained inclusions of chromite, carbonates and plagioclase (feldspathic glass and maskelynite) and submicron crystals of iron oxides and sulfides, predominantly magnetite and pyrrhotite (Mittlefehldt, 1994). The parent rock is understood to be compositionally similar to the shergottite meteorites and derived from a basaltic magma that settled on or near to the Martian surface with an igneous age around 4.1 Ga (Lapen et al., 2010). Recovered sections of the meteorite exhibit a number of shock-induced textures, characteristic of multiple generations of impact events during its time buried on Mars (Treiman, 1998, 2021; Fritz et al., 2005a).

The meteorite is cut by narrow bands of granular orthopyroxene and chromite, with disaggregated chromite grains in close proximity, suggesting an early impact capable of intense and complex material shear (Treiman, 1995). The equigranular texture of these bands was likely established in an extensive thermal event caused by this impact. We refer to this deformation event as D1, keeping the convention established by Treiman (1998). These granular bands predate the deposition

* Corresponding author.
E-mail address: t.north18@imperial.ac.uk (T.L. North).

https://doi.org/10.1016/j.icarus.2022.115322
Received 13 June 2022; Received in revised form 25 September 2022; Accepted 18 October 2022
Available online 25 October 2022

of carbonate material in the meteorite (Borg et al., 1999) and have an Rb–Sr age of approximately 4.0 Ga (Borg et al., 1999; Beard et al., 2013). A second, subsequent impact has been identified primarily by broken and fractured carbonate globules present in the rock (Mittlefehldt, 1994). Following the same convention, this is the D2 event. The fracturing of carbonates within the rock means D2 must post-date carbonate deposition within the meteorite. Further evidence includes the presence of silica, orthopyroxene and plagioclase glasses (Barber and Scott, 2006) and the formation of submicron magnetite by the decomposition of iron-rich carbonates (Treiman and Essene, 2011). Peak temperatures must have been capable of melting plagioclase into glass, although a shock pressure for the event is unknown.

Historically, the strength of these impacts has been determined by comparison to experimental data from terrestrial analogs that produce similar shock-textures or temperatures (Lambert and Grieve, 1984; Fritz et al., 2005b). However, when compared to terrestrial samples, the relationship between pressure and temperature has been shown to be very different on the sub-millimeter scale due to differences in both the mineral properties and the porosities of meteorites (Davison et al., 2017).

Paleomagnetic investigations of ALH 84001 have posited a long-lived (3.9–4.1 Gyr) natural remanent magnetization (NRM) that is heterogeneously oriented on the millimeter-scale and predominantly hosted in pyrrhotite present in carbonates and chromite-sulfide assemblages (Kirschvink et al., 1997; Antretter and Fuller, 2002; Antretter et al., 2003a; Weiss et al., 2000, 2002, 2004, 2008b; Steele et al., 2022). Below 40 °C, there is remanent magnetization acquired either during ejection (Weiss et al., 2002) or terrestrially in Antarctica (Antretter et al., 2003a). These observations support the hypothesis that the bulk meteorite has remained cold since it acquired its NRM, and that ALH 84001 experienced relatively low temperatures and pressures during its ejection (Weiss et al., 2000).

Heterogeneously oriented magnetizations, coupled with localized, intense and short-lived peak temperatures, point towards an unknown process able to produce strong thermal gradients on the grain-scale following an impact event. In this study we determine the thermodynamic response of a body like ALH 84001 to shock on the sub-millimeter scale. We present a suite of simulations of impacts on ALH 84001 using the iSALE-2D shock physics code (Collins et al., 2004; Wünnemann et al., 2006) to reconcile the independently reported shock and thermal histories of the meteorite, as well as offer insight into the feasibility of the heterogeneous impact remagnetization hypothesis (Weiss et al., 2008b; Steele et al., 2022).

2. Methods

To simulate the response of a meteorite sample such as ALH 84001 to impact, we designed a mesoscale numerical experiment that exposes the sample to a simplified shock loading process approximating that produced by an impact. In reality, impact-induced shock loading of a sample is complex and will depend on many factors, such as the size and speed of the impactor, the distance of the sample from the impact site and the nature of the target between the impact site and the sample. These factors affect the peak amplitude of the shock pulse, the duration (or dwell time) of the shock as well as the loading pattern. For a homogeneous target, the loading pattern may be a simple, almost planar shock pulse with a short rise time, but for a heterogeneous target with porosity, fractures and lithological changes, the loading pattern may be complex and involve a long rise time and/or several shock reverberations, with multiple directions.

For practical reasons, here we consider only a simple loading pattern of a quasi-planar shock wave with a relatively short (microseconds) duration. From high-resolution images of a thin section of ALH 84001, we constructed a synthetic approximation of the meteorite using its four major constituents. Appropriate material models for each component were selected. We then simulated the passage of quasi-planar shock waves of a range of different shock pressures (3–67 GPa) through this synthetic meteorite sample using the iSALE2D shock physics code (Collins et al., 2004; Wünnemann et al., 2006). We recorded the mesoscale thermodynamic and mechanical response of the synthetic meteorite sample to the shock loading and then modeled subsequent thermal equilibration by conduction. In the following sections we describe each of the steps in our procedure and the codes used.

2.1. The iSALE-2D shock physics code

An extension of the SALE hydrocode (Amsden et al., 1980), iSALE-2D is a multi-material, multi-rheology shock physics code (Collins et al., 2004; Wünnemann et al., 2006), benchmarked against other shock codes (Pierazzo et al., 2008) and validated against laboratory impact experiments (e.g. Pierazzo et al., 2008; Davison et al., 2011). Originally developed to study large-scale cratering, iSALE has recently been modified to examine the heterogeneous physical response of meteoritic materials to planar shock waves at the length scale of internal heterogeneities (Güldemeister et al., 2013; Davison et al., 2016; Derrick et al., 2019; Moreau et al., 2019). Such simulations are referred to as 'mesoscale' as they reveal phenomena present on an intermediate scale between the micro or atomic scale and the macro or bulk scale (e.g. Nesterenko, 2001; Borg and Vogler, 2008). Past meteorite studies have defined the mesoscale as fully resolving a chondrule, $\sim$ 10 μm (e.g. Bland et al., 2014; Moreau et al., 2019). In this study, we maintain the same order of magnitude as previous models and define the mesoscale as the resolution required to observe physical changes in the coarse inclusions within our samples (10-100 μm).

2.2. ALH 84001 as a four material system

Materials were selected on the basis of abundance and importance to our investigation. The criteria in our selection process aimed to replicate the natural heterogeneity of the system, while eliminating the rarest and smallest inclusions that would be difficult to adequately resolve ($\ll$ 10 μm). An example of how the synthetic sample was constructed from the meteorite thin-section is shown in Fig. 1. Consistent with our criteria, the mineralogy has been divided into four constituents: chromite (including iron oxides and sulfides), carbonate (coarse inclusions dominated by calcium carbonates), plagioclase (including maskelynite) and finally orthopyroxene, the bulk material.

2.3. Equations of state

Each of the constituent materials of ALH 84001 were described using the most appropriate material model available. In iSALE, the material model is defined by an Equation of State (EoS), which describes the response of a material to a change in volume, and a strength model, which describes the resistance of a material to changes in shape. The availability of accurate material models describing meteoritic components is limited. Therefore, we represented three of the four component materials with an equation of state using the closest analog material possible and strength model parameters representative of the material in question. For the fourth component material, chromite, we developed a new Tillotson EoS (Tillotson, 1962) for this study.

The EoS for chromite, $FeCr_2O_4$, represents the coarse chromite grains as well as the mixture of iron oxides and sulfides throughout the meteorite. As there is insufficient experimental shock data in the literature for chromite, the Tillotson parameters (a, b, α, β, B) were calculated by fitting to shock data for magnetite, Fe_3O_4, which is the predominant iron oxide found in the chromite inclusions (van Thiel et al., 1977; Marsh, 1980). The remaining Tillotson parameters and material constants (A, bulk modulus; E_0, E_{IV}, E_{C_V}, initial, incipient and complete vaporization energies, respectively; ρ_0, reference density; C_V, specific heat capacity) were chosen using available data for chromite (Klemme et al., 2000; Liu et al., 2016). Plagioclase was also described using a

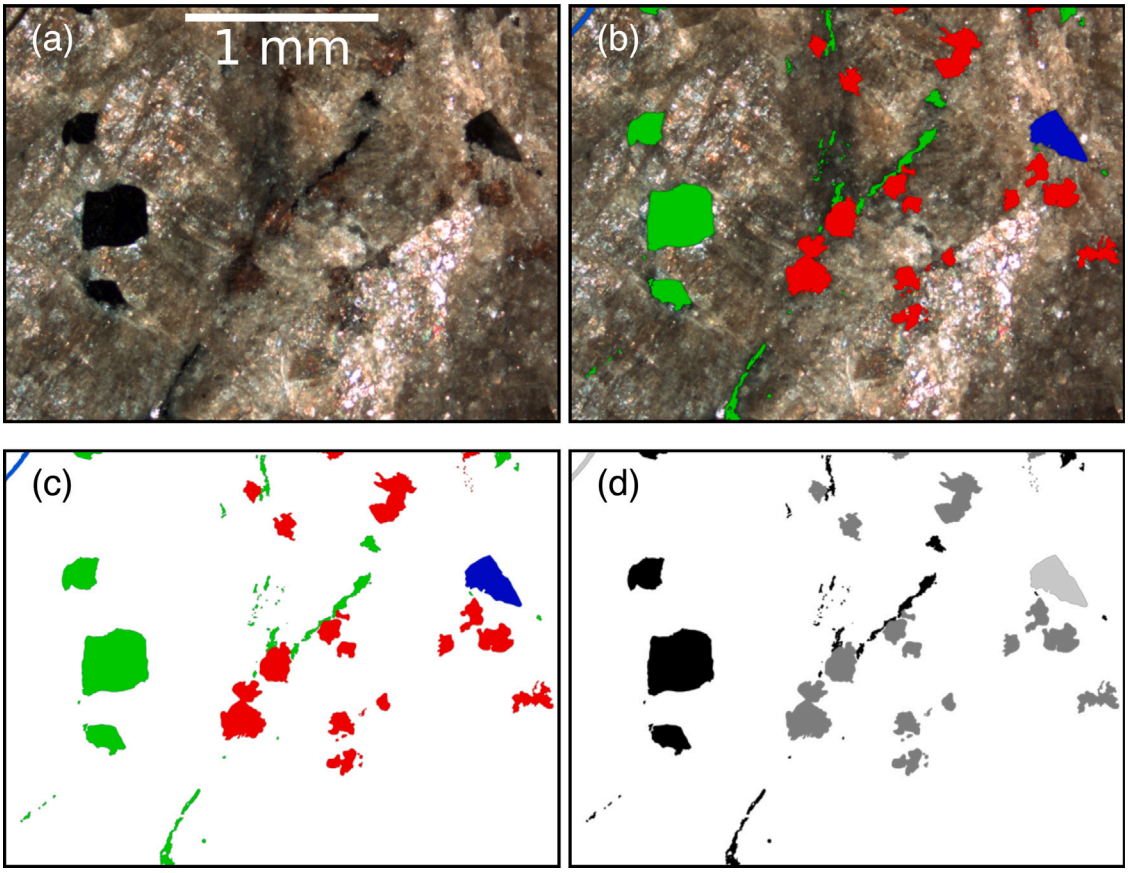

Fig. 1. Sample selection for one of the meteorite cross-sections. The original 6.4 mm^2 image is presented with a scalebar (a). The following three images demonstrate the identification of inclusions (b), the reduction to an RGB colormap (c; red: calcite; green: chromite; blue: gabbro; white: dunite) and finally the conversion to a grayscale image ready for use with iSALE-2D (d). (For interpretation of the references to color in this figure legend, the reader is referred to the web version of this article.)

Table 1
Tillotson parameters for the materials gabbroic anorthosite (O'Keefe and Ahrens, 1982) and chromite (developed for this study) which have been described using the Tillotson Equation of State.

Parameter	Gabbro	Chromite
a	0.50	0.50
b	1.45	0.47
α	5.00	5.00
β	5.00	5.00
A (Pa)	7.10×10^{10}	1.80×10^{11}
B (Pa)	7.50×10^{10}	1.78×10^{11}
E_0 (J/kg)	4.87×10^{6}	1.20×10^{7}
E_{IV} (J/kg)	4.72×10^{6}	3.00×10^{6}
E_{CV} (J/kg)	1.82×10^{7}	1.60×10^{7}

Tillotson EoS, with strength and material parameters fit to gabbroic anorthosite (O'Keefe and Ahrens, 1982). The Tillotson parameters used in this study for gabbroic anorthosite (gabbro hereafter) and chromite are summarized in Table 1.

Behavior of the carbonate and orthopyroxene were described using analytical equation of state (ANEOS)-derived tables for calcite (Pierazzo et al., 1998) and dunite (Benz et al., 1989), respectively. It is important to note that these are physical proxies and not chemical ones. Dunite, which is largely olivine (> 90%), has been used in place of an orthopyroxene because its EoS provides a better match to shock wave data for pyroxenite than an alternative, simplified EoS (Moreau et al., 2019).

2.4. Strength models

A pressure-, temperature- and strain-dependent strength model for geological materials (Ivanov et al., 1997; Collins et al., 2004) was used to describe the resistance of the carbonate, gabbro and dunite to shear deformation, while a constant-strength ductile model appropriate for metallic materials was used to describe the shear strength of chromite.

As ALH 84001 is understood to have suffered multiple impacts, the bulk rock material may have been damaged by impacts prior to the one(s) that produced the observed shock textures in the meteorite. In most of our simulations, we have assumed the dunite is intact, with its strength parameters fit to data for Horoman dunite (Shimada et al., 1983). However, to account for the possibility that the bulk material may have been weakened by previous impacts, our results also consider a second set of strength parameters that were determined by fitting the intact strength model envelope to strength data from a weaker Norwegian dunite, closer to peridotite (Murrell and Chakravarty, 1973; Ismail and Murrell, 1990). The fit to these models is displayed in Fig. 2; the coefficients are summarized in Table 2.

2.5. Simulation design

We examined the response of two cross-sections of ALH 84001 (S1 and S2 hereafter) to a planar impact using iSALE-2D. We consider the two cross-sections of ALH 84001 to be approximately representative of the bulk meteorite. The simulation mesh was generated from high-resolution images of the meteorite cross-sections where the pixels of each image became the cells of the mesh. The size of the meteorite cross-sections, which measured 2.93 mm × 2.20 mm for S1 and

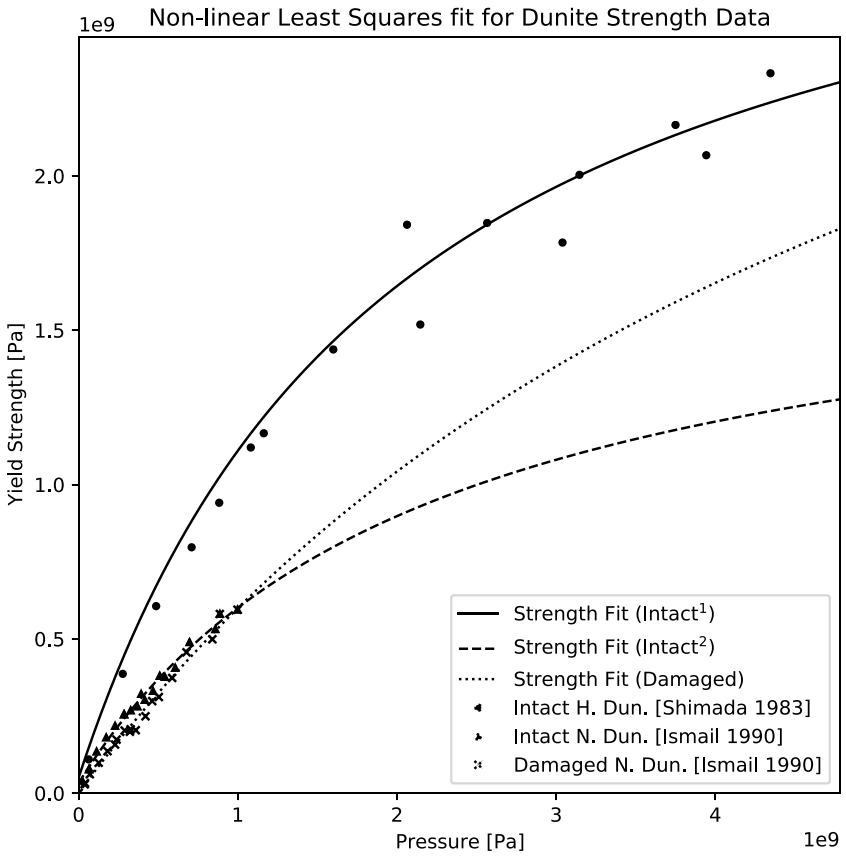

Fig. 2. Strength models calculated from two different dunite datasets. Shown are strength models for intact Horoman dunite that we have used in the majority of our simulations (Intact[1]) (Shimada et al., 1983), alongside a weaker strength model (Intact[2]) produced from shock data on Norwegian dunite (Ismail and Murrell, 1990). In addition, we include the strength model for damaged dunite which is common to both the intact models. The coefficients for the intact models are listed in Table 2.

Table 2
Parameters for the strength models we have fit to intact Horoman dunite (Shimada et al., 1983) and intact Norwegian dunite (Ismail and Murrell, 1990). μ_i is the coefficient of friction for intact rock while Y_{i0} and Y_{im} are material strength parameters. We have based the parameters for Horoman dunite on those used by Potter et al. (2012).

Parameter	H. Dun.	N. Dun.
μ_i	1.58	0.83
Y_{i0} (MPa)	50.7	33.3
Y_{im} (GPa)	3.26	1.85

4.04 mm × 3.33 mm for S2, were maintained using a mesh resolution (cell area) of 20 μm^2. This resolution meant we recorded an average of 75 cells per particle radius (CPPR) as measured in calcite.

To generate a quasi-planar shock wave in the simulated mesh produced from the meteorite cross-sections, impact experiments were performed where we collided an impactor with an initially stationary target, comprised of a sample plate sandwiched between a cover plate adjacent to the impactor and buffer plate (Davison et al., 2016). All four plates were made from identical material as a simple mechanism to mitigate unwanted reflections between plate boundaries. Moving with a given velocity, the impactor plate collided with the cover plate, producing a shock that traveled through it and into the sample (Fig. 3). The cover plate allowed the shock wave to reach a steady state before reaching the sample region. The shock then passed through the sample and into a buffer plate. Meanwhile, a release wave formed as the shock wave in the impactor plate reflected off the rear of the impactor. The release wave then passed back through the impactor, cover and sample plates. The simulation was allowed to run until the release wave had propagated all the way through the sample and it was released from its shocked state.

2.6. Lagrangian tracers

Response of the sample to the planar shock was measured using Lagrangian tracers placed in each computational cell of the mesh. Tracers were moved through the Eulerian computational grid according to material volume fluxes using the algorithm described in Davison et al. (2016) to ensure that they record information specific to the material they were initially assigned to. These tracers allowed us to record the thermodynamic and mechanical experience of the materials during the simulation, as well as to perform statistical analyses on a per-material basis from the model.

2.7. Shock wave amplitude

The amplitude (bulk pressure) of the shock was controlled by the velocity of the impactor. As dunite was the dominant material component, we were able to estimate the impact speed necessary for a given shock pressure using the relationship between the particle velocity and shock velocity in dunite. For the simulations presented in this work, we have impact velocities that range from 300 ms^{-1} to 4700 ms^{-1} which correspond to bulk pressures generated in the sample between 3 GPa and 67 GPa. Within this range, we have included simulations at significant thresholds for ALH 84001 such as at 15 GPa, the pressure estimate for an ejection event from Mars that would preserve the 40 °C 'cold' component of the remanence within the meteorite (DeCarli et al., 2007; Weiss et al., 2000), 33 GPa, the estimate bulk pressure experience of ALH 84001 from Fritz et al. (2005a) and 55 GPa, the maximum upper limit of the shock pressure reached during ejection as measured in Martian meteorite ALH77005 (Fritz et al., 2005a).

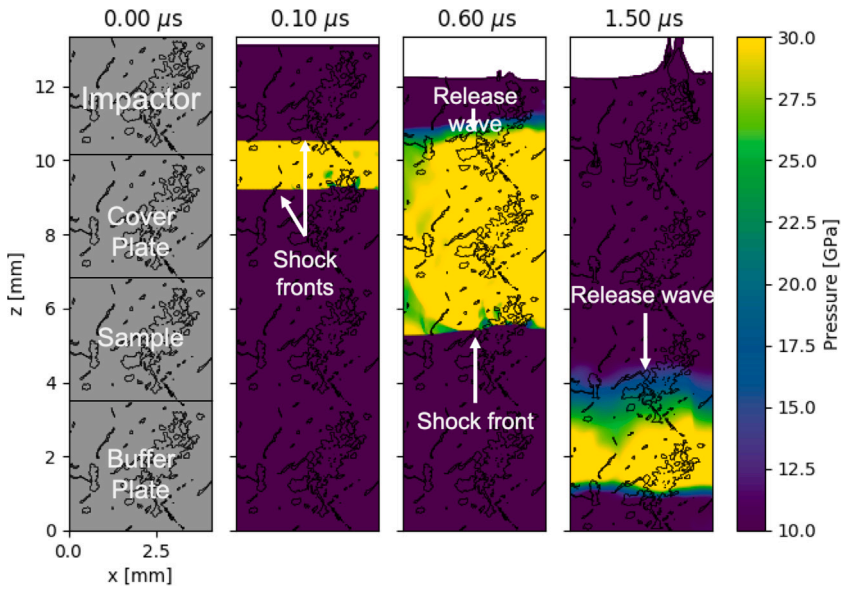

Fig. 3. The impact "sandwich" model shown for the larger S2 cross-section. In this simulation, the impactor, cover, sample and buffer plates are all identical. The impactor is given an initial velocity in the $-z$ direction causing a collision to occur at the impactor-cover plate boundary. This collision generates two shock waves — one in the cover plate traveling in the $-z$ direction causing the initial shock loading, and a second in the impactor plate traveling in the $+z$ direction. Once the shock wave reaches the top of the impactor, it reflects off the top of the impactor plate and travels in the $-z$ direction towards the sample, releasing material from a shocked state as it passes through.

2.8. Temperature nomenclature

In this study we refer to three distinct temperature measurements. The first is the maximum peak temperature. Peak temperature is the highest temperature experienced during passage of the shock wave, which can vary between materials and within grains of the same material. The maximum peak temperatures quoted in this study for a given material are the mean average of the hottest 1% of tracers in that material. The second important temperature is the average post-shock temperature. This is the average temperature recorded by tracers in a given material at the end of the iSALE-2D simulation, after the release wave has passed through the sample (approximately 1.1-1.2 μs after the beginning of the simulation in all cases). Finally, we define the "equilibrium temperature" of the meteorite as the temperature reached once the whole sample comes to thermal equilibrium. The peak and post-shock temperatures were calculated by iSALE-2D, while the equilibrium temperature was determined by a separate thermal equilibration calculation that accounted for cooling following an impact event.

2.9. Thermal equilibrium

To calculate thermal equilibration of the sample we used a finite-difference approach to solve the 2D heat equation

$$\frac{\partial U}{\partial t} = D\left(\frac{\partial^2 U}{\partial x^2} + \frac{\partial^2 U}{\partial y^2}\right) \tag{1}$$

where D is the diffusion coefficient, x and y are the 2D Cartesian coordinates of the mesh cells, t is time and $U(x, y, t)$ is the temperature field, which is initialized with the average post-shock temperature as calculated from our iSALE-2D simulation. Each cell in the mesh was assigned a diffusivity coefficient. To reduce the computational expense when solving Eq. (1), we adjusted the spatial resolution of the mesh to be two times coarser than the mesh output from the iSALE simulation. The coarsening algorithm assigned an initial temperature and diffusivity to each cell in a manner that conserved the mass and total internal energy of the iSALE-2D cells that are being combined. In other words, the new, 'coarsened' cell, has a diffusivity and specific heat capacity comprised of a mass weighted-average of the four cells of the overlapping iSALE-2D mesh.

Eq. (1) was solved using a simple forward-Euler integration in time. The maximum permissible timestep (Δt) without the equation becoming unstable is

$$\Delta t = \frac{1}{2D}\frac{(\Delta x \Delta y)^2}{(\Delta x)^2 + (\Delta y)^2} \tag{2}$$

The solution was allowed to run for a sufficient number of timesteps until the meteorite reached thermal equilibrium, defined as a change in thermal covariance across the sample of less than 0.1%. We treated the edges of the mesh using Neumann boundary conditions (zero temperature gradient normal to the boundary). Videos of the cooling process are included in the supplementary materials.

Thermochronology estimates of Martian paleotemperatures have shown ALH 84001 cannot have been at a constant long-term temperature greater than −60 °C to −70 °C since ~4 Ga (Shuster and Weiss, 2005). More recent studies have refined this constraint to have an even cooler upper limit of −63 °C (Min and Reiners, 2007). For our thermal equilibrium estimates, we have assumed the 'warmest-case scenario', having chosen the initial temperature of ALH 84001 to be −60 °C. In doing so, our estimates of equilibrium temperatures can be treated as conservative upper limits. As our iSALE-2D model was run using an initial temperature set to be the ANEOS reference temperature of 20 °C, we adjust the temperature output of each simulation by subtracting 80 °C at the start of the thermal equilibrium calculation.

3. Results

Across a number of different simulations, we varied impact velocities, meteorite composition, material strength and the orientation of the sample relative to the direction of the impact to investigate the length scale and heterogeneity of impact-induced thermal gradients within the meteorite. The results highlight the requirement for an appreciation of the mesoscale structure of meteorites which will, in turn, enable future studies to form more a complete understanding of their shock and thermal histories.

3.1. Reference simulations

We first present two simulations, one for each of our cross-sections (S1 and S2), where the sample experienced an average 'bulk' shock

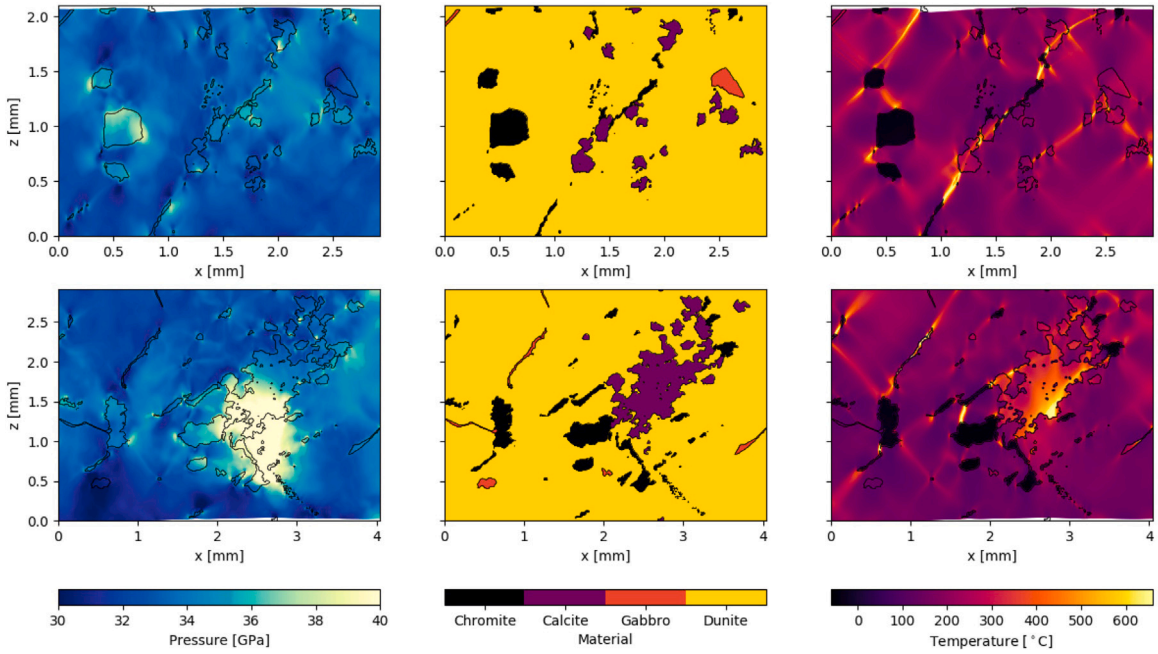

Fig. 4. Peak pressure (left), material (center) and post-shock temperature (right) colormaps, plotted from data recorded by Lagrangian tracers present within each cell of the mesh of the models. The upper three panes display the response of cross-section S1, while the lower three panes are the larger S2. The sharp linear features in the temperature colormaps point to the locations where material shear occurs. (For interpretation of the references to color in this figure legend, the reader is referred to the web version of this article.)

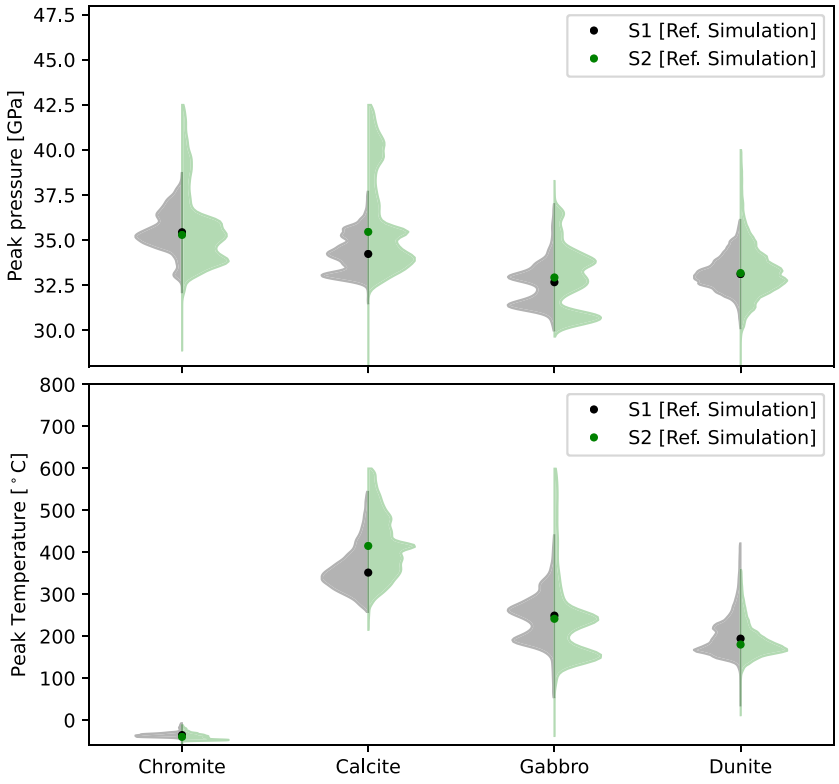

Fig. 5. Peak pressure experienced (top) and post-shock temperature (bottom) distributions of tracers in each material in the reference (33 GPa) simulations for S1 and S2. The marker centered on each of the distributions is the median average of the data. The plots have been trimmed to display all tracers within three standard deviations of the mean.

pressure of 33 GPa (corresponding to a plate impact velocity of 2720 ms^{-1}) in both cases. This shock pressure falls in the center of our investigated range. We will refer to these as the reference simulations.

In the reference simulations, both samples displayed spatially heterogeneous peak pressures and heating in response to the passage of the planar shock wave (Fig. 4, Fig. 5). We observed small variation in the average shock pressure experienced in the minor material constituents, from a minimum of 32.5 GPa (gabbro, S1) to a maximum of 36 GPa (calcite, S2), but the overall bulk pressure (33 GPa) is controlled by the major constituent, dunite (Fig. 5). Peak pressure highs are generally

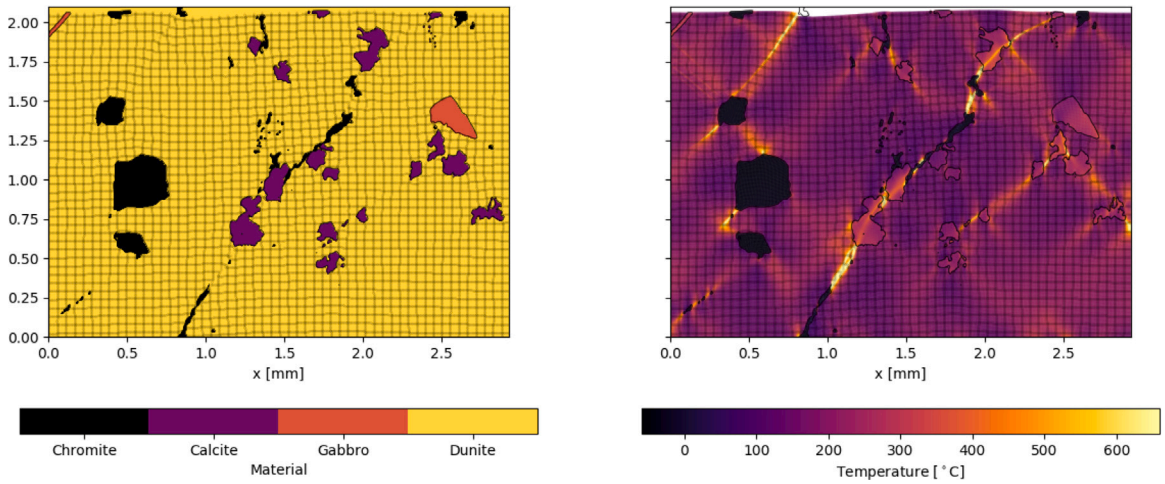

Fig. 6. Colormaps produced from the S1 reference simulation using Lagrangian tracers to identify the material locations and post-shock temperature. Included is a grid of tracers; each cell in the grid represents approximately 360 tracers. Warping of the grid represents areas of shear deformation whereby sections of material have shifted apart. (For interpretation of the references to color in this figure legend, the reader is referred to the web version of this article.)

associated with calcite and chromite regions which we have attributed to shock reverberations at material boundaries. However, the post-shock temperature varies considerably between the constituents and we observe a wide distribution of temperatures within each material (Fig. 5). While the average post-shock temperature in both reference simulations was 170 °C, the average post-shock temperature of each material varied from a minimum of −40 °C in the chromite to 370 °C in calcite.

Apart from chromite, we observe a broad distribution of temperatures around the median value. For example, while the response of the chromite is relatively consistent in both samples, the response of the calcite in S1 (Fig. 5) shows a broad range of post-shock temperatures. The median post-shock temperature is around 260 °C, while some of the calcite reached ~500 °C and other regions remained below 0 °C immediately following the impact. Calcite, which shows the greatest variability in temperature, exhibits no clear spatial pattern of heating. Some calcite regions are heated strongly, while others are hardly heated, particularly in S1 (Fig. 4). In dunite, on the other hand, there is clear pattern of heating, with narrow linear zones of strong heating separating regions of low to modest heating. Pressure fluctuations and reverberations caused by mesoscale heterogeneities and shear heating offer potential explanations for the observed spatial variation in heating.

3.2. Plastic deformation and shear heating in ALH 84001

Impact-induced heating originates from the work done by both the isotropic compression (PdV work) and shear deformation (plastic work) of material. To visualize shear deformation, we show a grid of the Lagrangian tracers over the sample images (Fig. 6). Regions of the grid appear dislocated where shear has occurred and these dislocations clearly correlate with the most intensely heated areas of the sample. This suggests that shear heating represents an important contribution to impact-related heating of ALH 84001 within the orthopyroxene (dunite) component and possibly the carbonate (calcite) component.

3.3. Influence of mesoscale structure

The orientation of the meteorite sample with respect to the propagation direction of shock waves that engulfed it while on Mars is unknown. Moreover, the composition of the rock material immediately adjacent to the sample is unknown, and therefore the shape of the shock front as it enters the sample is also not known. To verify that our results are not dependent on sample orientation or architecture of our simulations (the mesoscale structure of the impactor and/or cover plate), we investigated the effects of rotating the angle of the incident shock, omitting materials from the sample as well as changing the mesoscale structure within the cover and buffer plates.

3.3.1. Sample orientation

S1 was rotated in three orientations in addition to the default orientation: 30°, 60° and 90°. The size of the cross-section and relative abundance of each material was kept consistent by tiling the cross-section in a 3 × 3 grid. We then took a slice with the same dimensions as the original cross-section, rotated by the desired orientation.

When the sample was rotated relative to the original shock direction, we found low statistical variation between simulations (Fig. 7). Across the four orientations, the bulk pressure varied by $\Delta\sigma_p < 0.06$ GPa, while the difference in average post-shock temperature was found to be $\Delta\sigma_T < 2.8$ °C. The chromite remained much colder than the other materials with a consistent temperature increase in all orientations. The response of the gabbro material showed the most variation with shock wave orientation, though this was by far the most minor constituent in our samples and was inherently the most susceptible to variation owing to its situation in one corner of the sample. This suggests that while shock direction can influence the fate of individual grains the bulk constituents of the meteorite would have a similar experience regardless of the shock direction.

3.3.2. Sample composition

To understand which components exerted the dominant control on the thermal heterogeneity observed, we adjusted the mineralogy of the S1 sample in two simulations. We performed this by omitting the chromite for the first simulation, followed by omitting calcite in the next. In each case, we substituted the removed material with the major constituent, dunite.

We found shear heating still occurred when each of these materials was removed from the system, although the location of some shear zones was clearly influenced by the minor components (Fig. 8). Shear deformation occurred predominantly in the dunite, though the shear zone locality differed in places when minor components were omitted compared to the reference simulation. For example, a shear zone in the lower right corner of the reference simulation between calcite grains (Fig. 8a) is absent when the calcite grains are removed (Fig. 8c). This suggests that the weaker calcite grains can act as nucleation points for shear fractures. The same is true for the chromite grains. While the location of shear deformation changed with the mesoscale structure of the sample, we can expect material shear to have occurred throughout ALH 84001 and that it is not unique to the samples studied here.

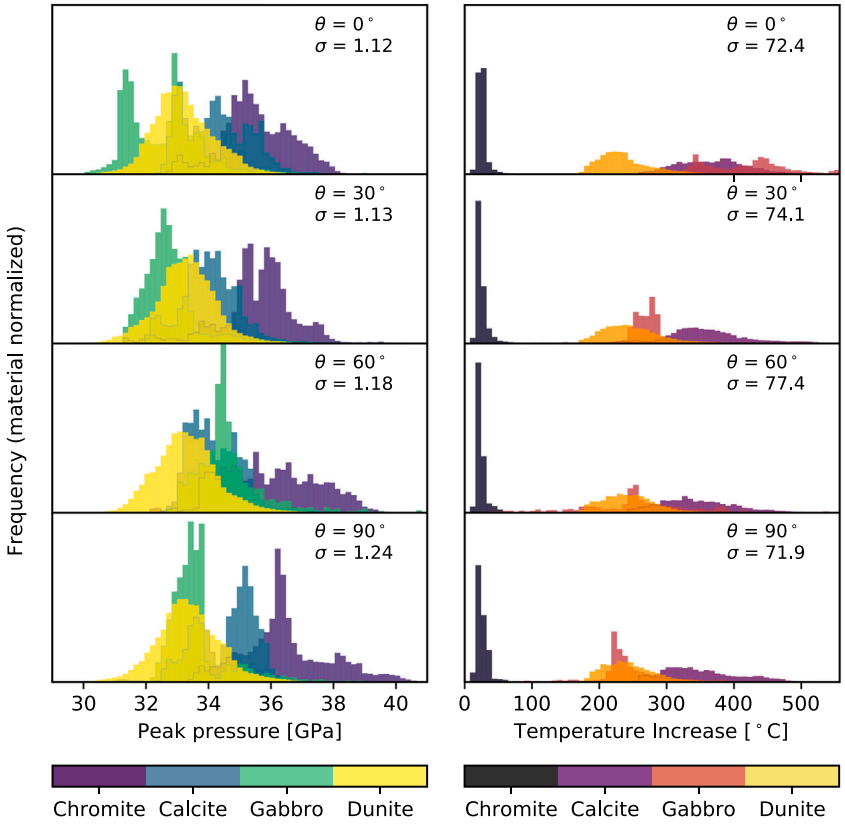

Fig. 7. Response histograms divided by material for the reference simulation ($\theta = 0°$) and three additional sample orientations, $\theta = 30°$, $60°$, $90°$. Each histogram has been normalized to have equal area. The left hand side displays the peak pressure experienced in each material while the right hand side is the post-shock temperature increase, measured once the release wave has passed through the sample. The standard deviation for the bulk response, σ, is included in each pane. The low statistical variability between models implies there is little affect in the orientation of the sample to our results.

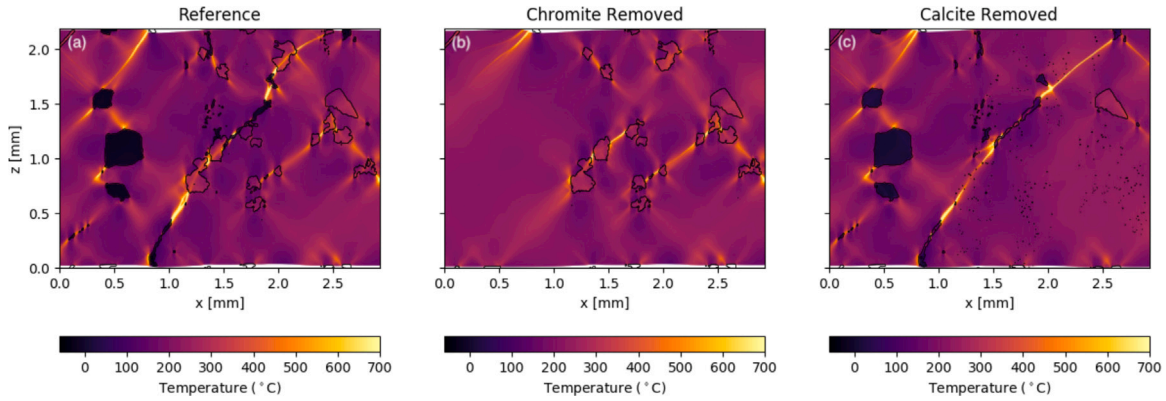

Fig. 8. Post-shock temperature maps produced for three different sample compositions for S1. We have reproduced the reference simulation for the four-material system (a) in addition to the response of the sample when chromite has been removed from the system (b), while (c) shows the response when calcite has been removed.

3.3.3. Plate mesoscale structure

As the structure of material immediately adjacent to the meteorite when in-situ on Mars is unknown, we examined the response of the sample to a change in the mesoscale structure of the cover plate in which the shock front is generated and reaches a quasi-steady state. This was achieved by rotating the cover plate 180°. This transformation maintained the proportions of the constituent materials relative to one another while the mesoscale structure of the cover plate as seen by the incoming shock wave was different. When compared to the reference simulation, this reversed-cover simulation showed that the pressure and temperature distributions were prone to small variations, particularly for the minor components, but the mean and range of the pressure and post-shock temperature remained consistent (Fig. 9).

3.4. Limiting shear strength

ALH 84001 exhibits evidence of multiple impacts while on Mars. To examine whether impact-related damage from one impact may alter the response of the meteorite material to subsequent impacts we also investigated the effect of the bulk strength of the meteorite on its response to shock. Our reference simulations used a strength model based on a relatively strong, intact Horoman dunite. To examine the effect of an impact-damaged orthopyroxene component of ALH 84001, we compared the reference simulation result to those from a simulation that employed strength model parameters appropriate for a weaker Norwegian dunite (Fig. 2).

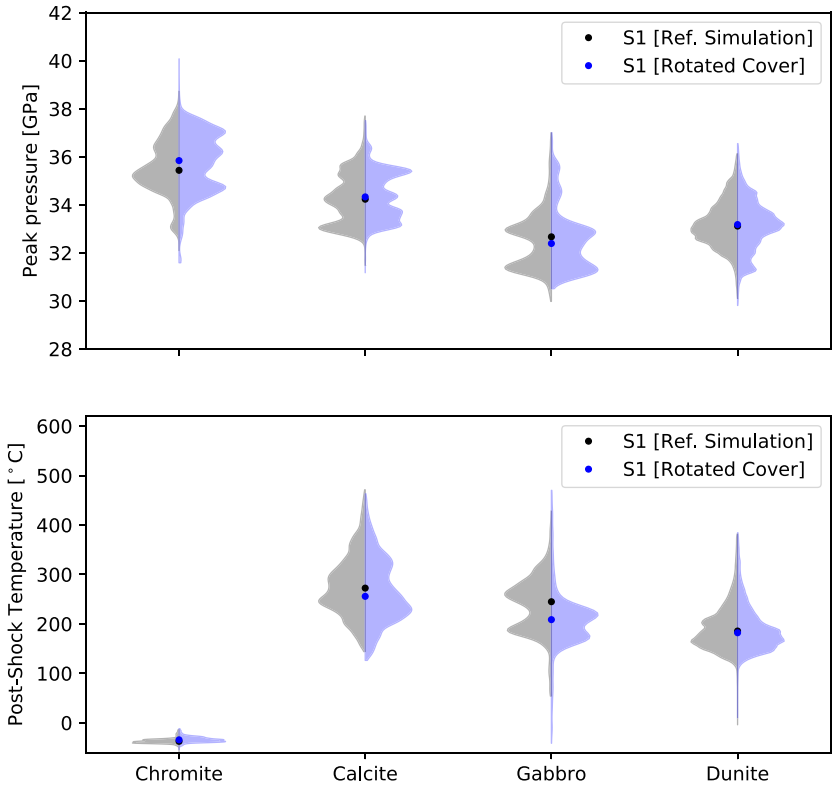

Fig. 9. Comparison of the 'rotated cover' plate result to the reference simulation. The rotated cover refers to the model where the cover plate has been rotated 180 degrees to demonstrate the effect of the shock wave passing through a different mesoscale structure. The shockfront that enters the sample is then slightly different to the one in the reference simulation.

Fig. 10 presents the comparison between two identical impact models where only the strength of the dunite has been changed. The initial conditions matched the reference simulation for S1. The impactor was set to have a velocity of 2720 ms^{-1} which produced an average bulk pressure of 33 GPa in the reference simulation, however, this generated a slightly greater bulk pressure of 34 GPa in the 'weak dunite' simulation. In contrast, while the average post-shock temperature in the reference simulation was 170 °C, we have found it to be lower using the Norwegian dunite at 130 °C. The difference in average post-shock temperature is due to the lower plastic work done in the Norwegian dunite when compared to the stronger Horoman dunite. The significantly higher post-shock temperature recorded in the stronger dunite further emphasizes the importance of shear heating to the overall impact heating of ALH 84001.

3.5. Temperature dependence on shock wave amplitude

By varying the plate velocity in our planar impact experiments, we simulated shock waves with twelve different bulk shock pressures between 3 GPa and 67 GPa. To quantify the effect of shock wave amplitude on heating in the sample, we were most interested in developing the relationship between the bulk shock pressure, peak temperature reached in each material and the equilibrium temperature reached by the meteorite. The post-shock temperatures in the sample at the end of the iSALE simulation were passed to the thermal equilibration code to determine the equilibrium temperature.

The relationship between the bulk pressure and equilibrium temperature of the sample is well-approximated by a linear fit above 22 GPa, while at lower pressures a non-linear polynomial (here we use a fifth-order polynomial) can adequately describe the trend (Fig. 11). However, the relationship between peak temperature and bulk pressure for individual constituent materials is more complex, non-linear and cannot be fully realized by looking at only the equilibrium temperature for the whole sample (Fig. 12).

Table 3
For a given bulk pressure, we present the maximum peak temperatures (T^{pk}) for each material alongside the equilibrium temperature (T^{eq}) of the sample. The peak temperature recorded in the calcite, gabbro and dunite is far greater than the equilibrium temperature in all cases. After the 8 GPa impact, the peak temperature recorded in chromite remains well below the equilibrium temperature.

Pressure (GPa)	T^{pk}_{chr} (°C)	T^{pk}_{cal} (°C)	T^{pk}_{gab} (°C)	T^{pk}_{dun} (°C)	T^{eq} (°C)
3	−34	35	−9	14	−56
5	−19	131	64	100	−50
7	−6	232	163	202	−36
8	−2	261	207	238	−28
13	1	350	298	349	3
16	1	399	356	421	31
24	6	494	456	571	107
33	12	657	481	671	186
40	23	908	572	758	249
49	81	1336	663	927	332
54	134	1605	849	1007	383
67	264	2188	1058	1171	514

In all the materials other than chromite, the maximum peak temperature experienced by a portion of the material is significantly greater than the equilibrium temperature measured in the sample (Table 3). While the chromite is heated by only tens of degrees for shock pressures below 50 GPa and subsequently warms up to reach the bulk temperature, the other materials are heated by hundreds of degrees and then rapidly cool to reach equilibrium (Fig. 13).

4. Discussion

Our suite of planar impact simulations demonstrate that the constituent materials of ALH 84001 can experience significantly different temperature–time paths to each other during an impact event. Our results reveal substantial intra- and inter-component variation in the maximum temperature increase generated by the impact.

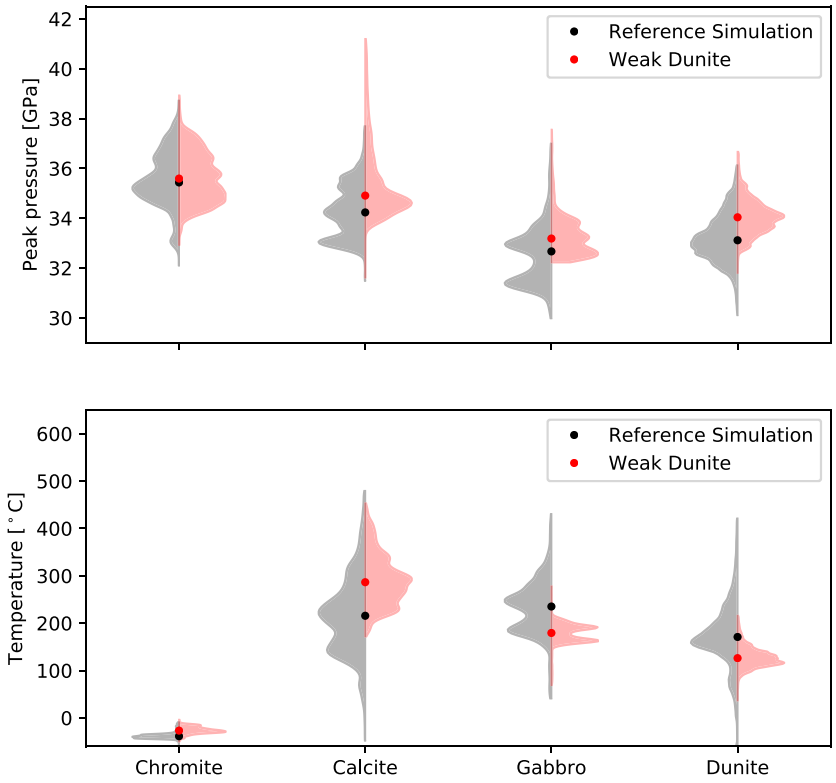

Fig. 10. Pressure and temperature distributions for each material in the reference simulation (using Horoman dunite) alongside the same impact using a weaker, Norwegian dunite. Both simulations shared the same architecture using the S1 cross-section and the impactor was given an initial velocity of 2720 ms^{-1}.

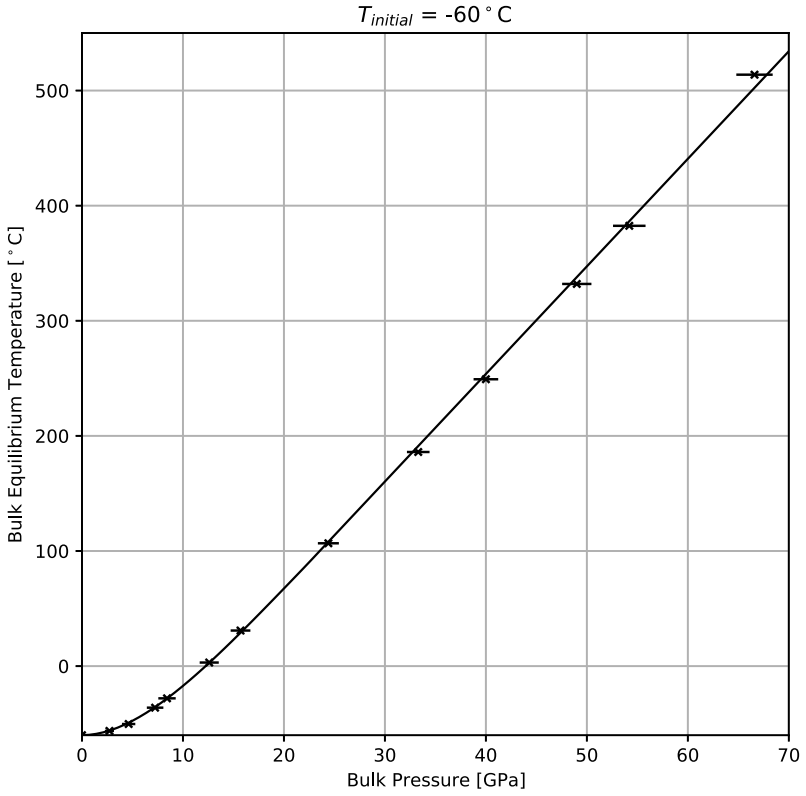

Fig. 11. The relationship between bulk shock pressure and equilibrium temperature of S1, shocked in the range 3–67 GPa. Below 22 GPa, the data is well-described by a polynomial fit, calculated using a non-linear least squares routine, fixed to intercept the axis at the initial simulation temperature, −60 °C. Above 22 GPa, the relationship becomes linear.

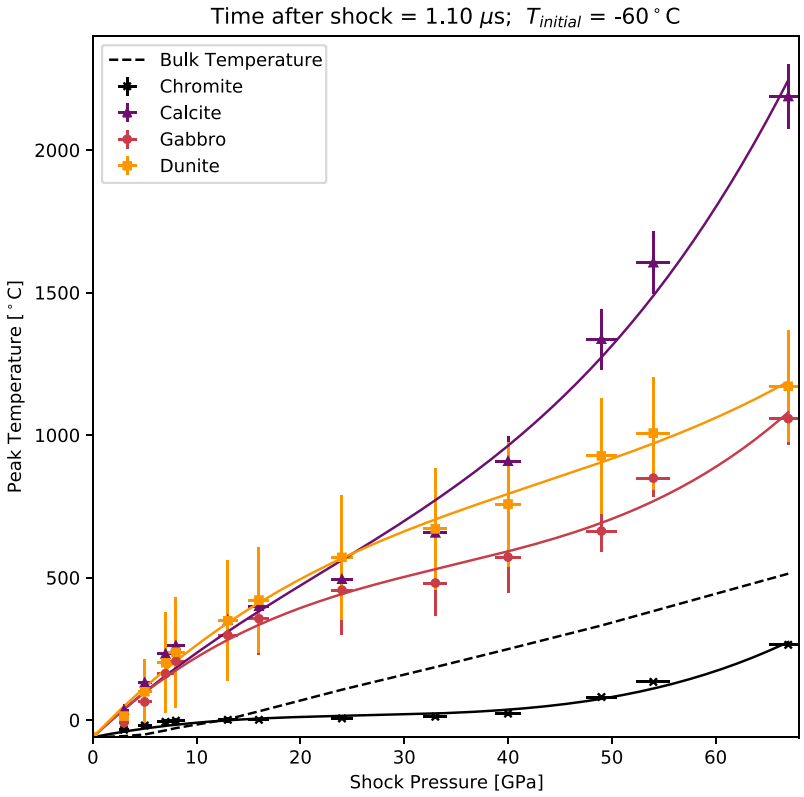

Fig. 12. Maximum peak temperatures measured in each of the constituent materials of ALH 84001 during impacts across a range of amplitudes. All curves are third-order polynomials fit to the data using a non-linear least-squares routine. Errors shown are one standard deviation of the thermal distribution for the given material. Additionally, the bulk temperature is plotted as a dotted line (this is the same as the line fitted to the data in Fig. 11).

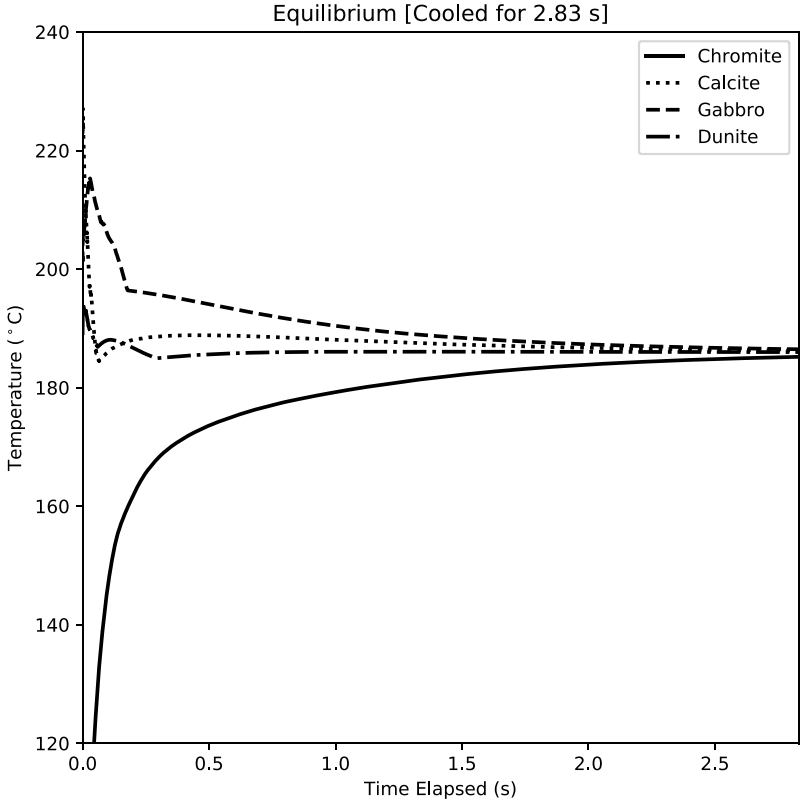

Fig. 13. Temperature–time path for each of ALH 84001's constituent materials immediately following the end of the 33 GPa reference simulation. Each of the four materials were allowed to cool until thermal equilibrium was reached; approximately 2.8 s after the release. Calculated using Eq. (2), the step size was 19.7 μs. The values that form the curves are the median temperature of each material.

4.1. A mechanism for heterogeneous heating

While evidence of shear deformation in ALH 84001 is well documented (Treiman, 1998; Barber and Scott, 2006; Treiman, 2021), the associated temperature increase attributed to the plastic work done in shearing has not been quantified. The importance of bulk shear heating during relatively low-velocity impacts on asteroids and other planetary bodies has recently been highlighted (Kurosawa et al., 2018, 2021). In this study we have found that shear heating can cause large temperature variations on the sub-mm scale in response to a quasi-planar shock wave. We have shown across a range of impacts similar to those that ALH 84001 would have been subject to, the meteorite would have experienced significant shear deformation and the associated heating would have produced strong thermal gradients on a sub-mm scale.

4.2. Thermal history recorded in magnetic carriers

The need for a mechanism that produces heterogeneous heating in the sample has been highlighted in previous paleomagnetic studies (Kirschvink et al., 1997; Antretter et al., 2003b; Weiss et al., 2008a), but until now, the physical process responsible had been unknown. The heterogeneous pattern of magnetization observed in the meteorite can be explained by thermal remagnetization of sub-volumes of the sample. The highly-localized, intense shearing we have observed in our simulations offers a mechanism that produces small regions of high temperature capable of remagnetizing these sub-volumes while not raising the rest of the sample to that temperature.

Magnetic reordering (the mechanism that allows the recording of an ancient magnetic field) occurs on timescales of nanoseconds, so even very brief transient heating events will overwrite existing NRMs within a sample. When examining the thermal evolution of the meteorite between the post-impact and thermal equilibrium temperatures, we found that in most parts of the sample, chromite warmed monotonically from its post-shock temperature to the equilibrium temperature. This shows that the temperature of the chromite, iron oxides and sulfides will rapidly (<3 s, plus shock wave dwell time) equilibrate via thermal diffusion. In this case, to overprint an existing NRM in the sample would require a shock event that heated the entire sample to an equilibrium temperature above the Curie temperature and all chromites would record the same magnetization direction.

On the other hand, an important consequence of the heterogeneous heating that we observe in our simulations of ALH 84001 is that in chromite grains next to shear zones, heat transfer from the shear zone into the chromite grain can lead to transient, local temperature excursions where the chromite was rapidly heated and then dropped back to the equilibrium temperature (Fig. 14; see also videos in supplementary materials). In other words, small chromite grains in shear zones or portions of larger grains near shear zones can be heated briefly to temperatures exceeding the equilibrium temperature. This means a single impact can demagnetize or remagnetize sub-volumes of the meteorite: some magnetic assemblages near shear zones may be partially demagnetized or even remagnetized, should the maximum temperature exceed the Curie point, while other magnetic carriers that are isolated from shear zones will be unaffected (if the equilibrium temperature is below the Curie point). In our 'reference simulation' (bulk pressure 33 GPa), approximately 22% of the simulation domain is above 320 °C once the meteorite is released from its shocked state. However, as shown in Fig. 14, the chromites that are re- or demagnetized are actually heated by nearby shear zones during thermal equilibration. If the magnetic carriers are small and uniformly distributed throughout the sample, then approximately the same proportion of magnetic carriers are potentially re- or demagnetized. On the other hand, if the magnetic carriers are preferentially located close to the shear zones, this fraction could be much higher.

4.3. Effect of shock pulse width on heterogeneous heating

The design of our simulation means that the shock pulse width (the duration the sample is in a shocked state) is much shorter than the time taken for the sample to reach thermal equilibrium. While the shock duration was around ~1 μs, thermal equilibrium was reached on a timescale of ~1–3 s after the passage of the release wave through the sample. This provides the opportunity for small grains within the meteorite to experience brief shock- or shear-induced high-temperature excursions prior to thermal equilibration. On the other hand, if the impact produces a shock pulse with a similar duration to the equilibrium timescale, thermal equilibration would occur whilst the meteorite is still being shocked and sheared. In this case, we anticipate heterogeneous heating will still occur, but the variance of peak temperature among different components will be reduced.

Shock pulse duration can be approximated by the impactor size divided by the impact speed. So for a typical impact speed on Mars of 10 km/s, we anticipate that cm-scale impactors would produce a shock wave similar to those we observe in our simulations. On the other hand, using the same impactor speed, impactors several hundred meters in size or larger would produce a shock duration comparable to the thermal equilibration timescale, which may diminish the thermal heterogeneity we observe for smaller impactors. Additional simulations to explore the influence of shock (and shear) duration on the variance of thermal heterogeneity would be valuable.

4.4. Constraints on shock history from paleomagnetism

The chromite-sulfide assemblages in ALH 84001 have been shown to record two distinct, statistically significant magnetization directions, which have been interpreted as evidence of at least two separate high-temperature deformation events in the presence of a martian surface magnetic field prior to 3.9 Ga (Weiss et al., 2002; Antretter et al., 2003a). The first of these magnetization directions, the primary magnetization, can be explained as a remanence from the Martian dynamo field at 4.1–4.0 Ga, recorded uniformly in chromite-sulfide assemblages throughout the meteorite (Weiss et al., 2008b). The recording of the primary magnetization would have required the temperature of the whole parent rock to exceed the Curie point of the pyrrhotite present in the chromite-sulfide assemblages, > 320 °C (Dunlop and Özdemir, 1997), which dominates the stable component of the NRM (Weiss et al., 2008b; Steele et al., 2022). The second of these magnetization directions is then a partial remagnetization where sub-volumes of the meteorite were remagnetized at a later time, around 3.9 Ga, where the change in direction is possibly a record of the Martian dynamo polar reversal (Steele et al., 2022). To account for only partial remagnetization, this second impact must have allowed a fraction of the sulfides in the rock to exceed 320 °C, while the equilibrium (bulk) temperature remained below the Curie temperature.

Also present in the meteorite is an incoherent pattern of weakly magnetized chromites and carbonates (Kirschvink et al., 1997; Antretter and Fuller, 2002; Weiss et al., 2002). This has been interpreted as evidence for a third, late impact event (D3) after the dynamo's cessation that demagnetized sub-volumes of the meteorite where some fraction of the magnetic carriers experienced very brief high-temperature excursions (Weiss et al., 2008b; Cassata et al., 2010) that were again insufficient to reset the NRM hosted elsewhere in the meteorite.

The paleomagnetic literature therefore impose the following constraints on the shock history of ALH 84001:

1. The first impact must have been sufficiently strong to raise the equilibrium temperature of the meteorite well in excess of 320 °C.
2. The second, and possibly third, impact allowed a fraction of the chromites in the rock to exceed 300 °C, but the equilibrium temperature remained below this temperature.
3. Since the first impact, the equilibrium temperature cannot have been raised above 300 °C, else the NRM would have been completely reset.

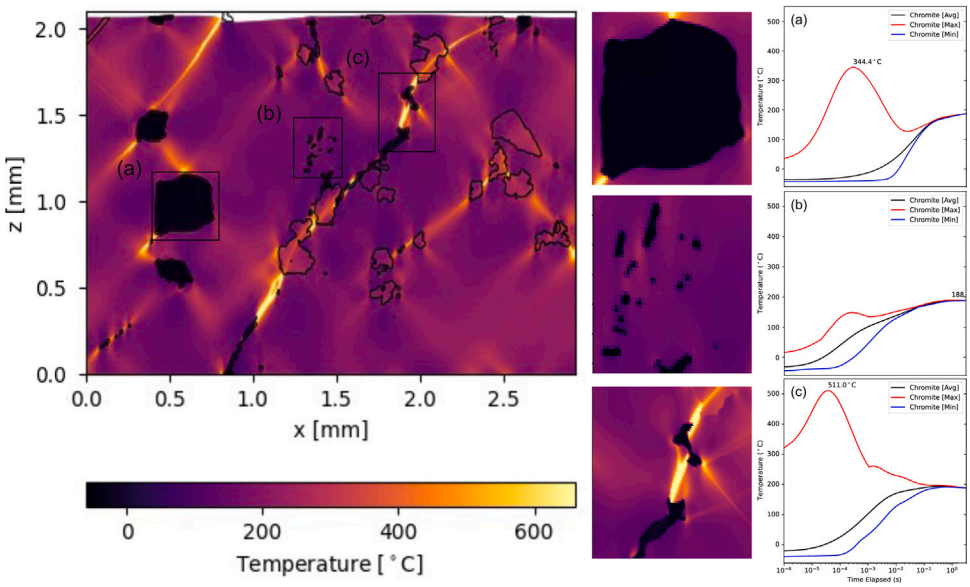

Fig. 14. This figure demonstrates the thermal evolution of three areas of the reference simulation for cross-section S1. We have chosen three grains characteristic of the chromite inclusions we observe in the sample; (a) shows a large, coarse inclusion, (b) is an assemblage of grains several microns across and (c) is a vein of chromite located in a shear zone. We see that the chromite close to shear zones experience temperature maxima greater than the post-shock temperature and the thermal equilibrium temperature.

4.5. New constraints on the shock history of ALH 84001

4.5.1. Early shock events

When combined with these paleomagnetic constraints, our simulation results can provide new constraints on the shock history of ALH 84001. The D1 event resulted in the granular bands seen throughout the meteorite, metamorphism above 875 °C, and full remagnetization of the chromite-sulfide assemblages (Treiman, 1995, 2021). Our results suggest that for D1 to have raised the temperature of the meteorite well in excess of 320 °C required a minimum shock pressure between 45–50 GPa. This is a conservative limit on the minimum bulk pressure as evidence attributed to D1 includes possible local bulk rock melting, requiring peak pressures in excess of 75 GPa (Treiman, 1998).

To achieve subsequent partial remagnetization of the sample, our results suggest that the D2 event was associated with a bulk shock pressure between 25–45 GPa. This range is compatible with small volumes of the sample experiencing the minimum shock pressure required to produce glass formed through shock-induced melt (40–45 GPa; Stöffler et al., 1991, Fig. 5) as well as the conversion of plagioclase to maskelynite which occurs in shocks in excess of 31 GPa (Kring et al., 1998; Treiman, 2021). Moreover, a shock wave of this amplitude would heat some fraction of the chromite-sulfide assemblages above ~ 320 °C allowing them to be remagnetized, while the remaining fraction would remain below 320 °C and retain its earlier magnetization.

4.5.2. "Recent" shock events

Evidence for a significant impact since 3.9 Ga is more equivocal and is not easily explained by our model results. The D3 event may be responsible for demagnetization of sub-volumes of the meteorite and has been identified by an Ar–Ar kinetic crossover around 1.16 Ga (Cassata et al., 2010). According to this analysis, the apparently more complete degassing of orthopyroxene compared to plagioclase in multiple aliquots of ALH 84001 recording a 1.16 Ga plateau age is best explained by rapid (~1 s) heating up to and above 1400 °C.

Adopting this temperature constraint, our simulation results are unable to explain the persistence of multiple generations of prior magnetization. The minimum pressure required to produce peak temperatures in gabbro (our analog for plagioclase) around 1400 °C is in excess of 60 GPa. At such pressures, the equilibrium temperature would be at least 440 °C, well above the Curie temperature of chromite-sulfide assemblages, which would reset all the paleomagnetic data stored in these carriers. Furthermore, shock pressures in excess of 50 GPa are likely to produce molten flowed quartz and feldspar, making it highly unlikely the carbonates present in the meteorite would have survived intact (Kring et al., 1998). Finally, this 1.16 Ga plateau is fully present in only a single Ar–Ar aliquot while a 4.0–3.9 Ga plateau, likely associated with the D2 event, is prominent in a majority of analyzed ALH 84001 material (Turner et al., 1997; Cassata et al., 2010). Several such Ar–Ar aliquots show virtually undisturbed ~3.9 Ga plateaus. A D3 event in excess of 60 GPa would be significantly stronger than estimates for the D2 event given above, contradicting the relative strengths of these events inferred from Ar–Ar data. Together, these observations suggest that simultaneous peak heating of orthopyroxene and plagioclase up to 1400 °C during the D3 event is unlikely. In any case, a recent study of terrestrial impact material, analogous to Martian shergottite meteorites, has shown the classical interpretation of argon ages recovered from impact sites can be unreliable without proper context (Jaret et al., 2018).

An alternative interpretation of the 1.16 Ga Ar–Ar plateau data is that differential degassing of orthopyroxene and plagioclase may have been due to heterogeneous heating instead of a kinetic crossover. The 1400 °C peak temperature estimate from the kinetic crossover analysis assumes that the plagioclase and orthopyroxene were both heated to this temperature. Our simulation results show that orthopyroxene can be heterogeneously heated to 100 – 200 °C above plagioclase separated at the sub-millimeter scale (Fig. 4). If this occurred during the D3 event, the peak temperature for plagioclase can be several hundred degrees below 1400 °C while still degassing less than nearby orthopyroxene. With the most favorable modeled diffusion domain sizes, orthopyroxene heated to ~ 1050 °C can degas at a similar rate as plagioclase heated locally to ~ 900 °C (Cassata et al., 2010, Fig. 6A). Under this favorable scenario, we are able to realize a peak temperature of ~ 1050 °C in the bulk rock material within a 1σ uncertainty in a 45 GPa impact. At this shock pressure, the equilibrium temperature is 300 °C and chromite-sulfide assemblages would not be completely remagnetized.

To further aid in explaining the locally extensive degassing event at 1.16 Ga, there may be a heating mechanism present not accounted for in our simulations. One possibility is the crushing out of pore space in the meteorite, responsible for the melting of gabbro. Compaction of a porous target would consume extra work during shock passage,

resulting in higher localized temperatures surrounding the collapsed pore (Wünnemann et al., 2006; Güldemeister et al., 2013). When combined with shear heating, it could be possible this would raise the temperature of very localized regions in the meteorite significantly, producing localized excess orthopyroxene degassing at 1.16 Ga, as observed. However, as the porosity history of the meteorite is unknown, we cannot provide further evidence in this study.

4.6. Ejection from Mars

Cosmic ray ages of ALH 84001 have dated the ejection of the meteorite from Mars to around 14 Ma (Eugster et al., 1997). Previous studies have shown the minimum shock pressure required to eject material from Mars to be around 10 GPa (Artemieva and Ivanov, 2004), however the upper limit on the ejection pressure of ALH 84001 is unclear. Previous studies have suggested that some material in the meteorite reached peak temperatures around 430 °C (Min and Reiners, 2007), while other studies have suggested that "cold" paleomagnetic data preserved in the meteorite required the equilibrium temperature to remain below 40 °C (Weiss et al., 2000). It is unclear if this cold magnetization component was acquired during ejection from the Martian surface or if it is actually a viscous remanent magnetization (VRM) acquired on Earth (Antretter et al., 2003a). Using Fig. 12, we find an upper limit on the impact pressure to be 16 GPa to be consistent with both of these observations. In a 16 GPa impact, the maximum peak temperature experienced by any material in the meteorite is 430 °C, while the equilibrium temperature remains just below 40 °C.

Our results can reconcile these observations to determine a 10–16 GPa "launch window" that satisfies both constraints. This window corresponds to equilibrium temperatures of −17 °C and 40 °C, with peak temperatures in dunite of 260 °C at 10 GPa, and 430 °C at 16 GPa.

5. Conclusions

Through a suite of mesoscale shock wave simulations, we have quantified the thermodynamic and physical response of Martian meteorite ALH 84001 to strong planar shock waves, similar to those it would have experienced before and as it was ejected from Mars. Over a range of shock pressures between 3 GPa and 67 GPa, our results show that ALH 84001 would likely have experienced strong syn-impact thermal heterogeneity on the sub-millimeter mesoscale. The physical mechanisms responsible for these steep thermal gradients are localized shear, occurring predominantly in the orthopyroxene component, and shock fluctuations and reverberations caused by the spatial variation in material properties within the sample.

We have attempted to reconcile the thermal constraints placed on the meteorite in paleomagnetic studies and petrologic observation, by measuring the peak, post-shock and thermal equilibrium temperatures following an impact experienced by different components of the meteorite, including its magnetic carriers. Our results provide several new constraints on the impact history of ALH 84001:

1. Granular bands were formed in an early impact D1 with a minimum shock pressure between 45–50 GPa.
2. Impacts after the first major shock event were weaker and therefore must have exerted a bulk shock pressure less than 45 GPa to retain the magnetization associated with D1.
3. The second major impact D2 that fractured carbonates throughout ALH 84001 must have a shock pressure in the range 25–45 GPa.
4. Our simulation results are difficult to reconcile with an event around 1.16 Ga that produced Ar degassing consistent with peak temperatures in excess of 1400 °C.
5. For event D3, our simulations suggest the differential heating of plagioclase and orthopyroxene in a 45 GPa shock event can tenuously explain both paleomagnetic and Ar–Ar thermochronometry data in the most extreme outliers.
6. If "cold" paleomagnetic data in the meteorite is not a VRM acquired on Earth, the maximum pressure upon ejection from Mars was 16 GPa.

The results presented here have wider implications for the meteorite record. We have demonstrated that peak temperatures recorded in some meteoritic materials are not representative of the thermal history of the bulk sample and might lead to misinterpretation of a meteorite's metamorphic history. This is especially pertinent for paleomagnetic investigations where ferromagnetic populations are remagnetized at different times and may hold record of different ancient paleofields. Our results emphasize the value of examining Martian meteorites on a per-material basis at the mesoscale, and highlight a need to incorporate the effects of heterogeneous heating, including heating by shear deformation, into the general shock classification of meteorites.

Data availability

Our iSALE-2D input files are available under http://dx.doi.org/10.5281/zenodo.6637894.

Acknowledgments

We would like to thank J. Derrick for developing the PySALESetup module (https://github.com/jgd10/PySALESetup) that was used to generate the initial mesh geometry from meteorite images. We also thank B. Johnson, B. Ivanov and one anonymous reviewer for their insightful comments that have helped in finalizing this study. We thank the developers of iSALE (www.isale-code.de), including K. Wünnemann, D. Elbeshausen, J. Melosh and B. Ivanov. T. N. was supported by Science and Technology Facilities Council for the funding of this project (ST/S505420/1).

Appendix A. Supplementary data

The video demonstrates the temperature evolution of the whole sample immediately following the passage of a planar shockwave. The simulation displayed is the 33 GPa 'reference' simulation. Temperature arrays were calculated according to the heat equation described in equation 1 in the article, while the timestep dt between calculations was $\Delta t/5$, where Δt was calculated according to equation 2 in the article.

(a) Displays the temperature map of all materials within the sample and is colored relative to the equilibrium temperature (186 °C).

In pane (b) we have colored all non-chromite material gray to show a comprehensive overview of the thermal experience in chromites throughout the sample. In doing so we highlight the spatially heterogeneous nature of the heating where chromites in shear zones (such as the chromite circled) experience secondary maxima, while the average chromite temperature remains below the thermal equilibrium temperature.

(c) describes the evolution of both the peak and average temperature recorded in the circled chromite, compared to the average temperature recorded in all chromites.

(d) is a close-up view of the circled chromite. We observe that the fringes connected to the shear zone in dunite are heated most of all, while the center heats up over a period of milliseconds.

Supplementary material related to this article can be found online at https://doi.org/10.1016/j.icarus.2022.115322.

References

Amsden, A.A., Ruppel, H.M., Hirt, C.W., 1980. SALE: A Simplified ALE computer program for fluid flow at all speeds. In: Los Alamos National Laboratories Report. Technical Report LA-8095 June, Los Alamos Scientific Laboratory, p. 101. http://dx.doi.org/10.2172/5176006, URL http://www.iaea.org/inis/collection/NCLCollectionStore/_Public/11/571/11571883.pdf?origin=publication_detail.

Antretter, M., Fuller, M., 2002. Paleomagnetism and rock magnetism of martian meteorite ALH 84001. Phys. Chem. Earth 27 (25–31), 1299–1303. http://dx.doi.org/10.1016/S1474-7065(02)00134-1.

Antretter, M., Fuller, M., Scott, E., Jackson, M., Moskowitz, B., Solheid, P., 2003a. Paleomagnetic record of Martian meteorite ALH84001. J. Geophys. Res. E: Planets 108 (6), http://dx.doi.org/10.1029/2002je001979.

Antretter, M., Fuller, M., Scott, E., Jackson, M., Moskowitz, B., Solheid, P., 2003b. Paleomagnetic record of Martian meteorite ALH84001. J. Geophys. Res. E: Planets 108 (6), 5049. http://dx.doi.org/10.1029/2002je001979.

Artemieva, N., Ivanov, B., 2004. Launch of martian meteorites in oblique impacts. Icarus 171 (1), 84–101. http://dx.doi.org/10.1016/j.icarus.2004.05.003.

Barber, D.J., Scott, E.R., 2006. Shock and thermal history of Martian meteorite Allan Hills 84001 from transmission electron microscopy. Meteorit. Planet. Sci. 41 (4), 643–662. http://dx.doi.org/10.1111/j.1945-5100.2006.tb00487.x.

Beard, B.L., Ludois, J.M., Lapen, T.J., Johnson, C.M., 2013. Pre-4.0 billion year weathering on Mars constrained by Rb-Sr geochronology on meteorite ALH84001. Earth Planet. Sci. Lett. 361, 173–182. http://dx.doi.org/10.1016/j.epsl.2012.10.021.

Benz, W., Cameron, A.G., Melosh, H.J., 1989. The origin of the Moon and the single-impact hypothesis III. Icarus 81 (1), 113–131. http://dx.doi.org/10.1016/0019-1035(89)90129-2.

Bland, P.A., Collins, G.S., Davison, T.M., Abreu, N.M., Ciesla, F.J., Muxworthy, A.R., Moore, J., 2014. Pressure-temperature evolution of primordial solar system solids during impact-induced compaction. Nature Commun. 5, 5451. http://dx.doi.org/10.1038/ncomms6451.

Borg, L.E., Connelly, J.N., Nyquist, L.E., Shih, C.Y., Wiesmann, H., Reese, Y., 1999. The age of the carbonates in martian meteorite ALH84001. Science 286 (5437), 90–94. http://dx.doi.org/10.1126/science.286.5437.90, URL https://pubmed.ncbi.nlm.nih.gov/10506566/.

Borg, J.P., Vogler, T.J., 2008. Mesoscale calculations of the dynamic behavior of a granular ceramic. Int. J. Solids Struct. 45 (6), 1676–1696. http://dx.doi.org/10.1016/j.ijsolstr.2007.10.027.

Brearley, A.J., 2003. Magnetite in ALH 84001: An origin by shock-induced thermal decomposition of iron carbonate. Meteorit. Planet. Sci. 38 (6), 849–870. http://dx.doi.org/10.1111/j.1945-5100.2003.tb00283.x.

Cassata, W.S., Shuster, D.L., Renne, P.R., Weiss, B.P., 2010. Evidence for shock heating and constraints on Martian surface temperatures revealed by 40Ar/39Ar thermochronometry of Martian meteorites. Geochim. Cosmochim. Acta 74 (23), 6900–6920. http://dx.doi.org/10.1016/j.gca.2010.08.027, URL www.elsevier.com/locate/gca.

Collins, G.S., Melosh, H.J., Ivanov, B.A., 2004. Modeling damage and deformation in impact simulations. Meteorit. Planet. Sci. 39 (2), 217–231. http://dx.doi.org/10.1111/j.1945-5100.2004.tb00337.x, URL http://doi.wiley.com/10.1111/j.1945-5100.2004.tb00337.x.

Davison, T.M., Collins, G.S., Bland, P.A., 2016. Mesoscale Modeling of Impact Compaction of Primitive Solar System Solids. Astrophys. J. 821 (1), 68. http://dx.doi.org/10.3847/0004-637X/821/1/68, http://arxiv.org/abs/1603.00376%0Ahttp://dx.doi.org/10.3847/0004-637X/821/1/68.

Davison, T.M., Collins, G.S., Elbeshausen, D., Wünnemann, K., Kearsley, A., 2011. Numerical modeling of oblique hypervelocity impacts on strong ductile targets. Meteorit. Planet. Sci. 46 (10), 1510–1524. http://dx.doi.org/10.1111/j.1945-5100.2011.01246.x, URL https://ui.adsabs.harvard.edu/abs/2011M&PS...46.1510D/abstract.

Davison, T.M., Derrick, J.G., Collins, G.S., Bland, P.A., Rutherford, M.E., Chapman, D.J., Eakins, D.E., 2017. Impact-induced compaction of primitive solar system solids: The need for mesoscale modelling and experiments. In: Procedia Engineering, Vol. 204. pp. 405–412. http://dx.doi.org/10.1016/j.proeng.2017.09.801, URL https://linkinghub.elsevier.com/retrieve/pii/S187770581734362X.

DeCarli, P.S., Goresy, A.E., Xie, Z., Sharp, T.G., 2007. Ejection mechanisms for Martian meteorites. In: AIP Conference Proceedings, Vol. 955. pp. 1371–1374. http://dx.doi.org/10.1063/1.2832979.

Derrick, J.G., Rutherford, M.E., Chapman, D.J., Davison, T.M., Duarte, J.P.P., Farbaniec, L., Bland, P.A., Eakins, D.E., Collins, G.S., 2019. Investigating shock processes in bimodal powder compaction through modelling and experiment at the mesoscale. Int. J. Solids Struct. 163, 211–219. http://dx.doi.org/10.1016/j.ijsolstr.2018.12.025.

Dunlop, D., Özdemir, Ö., 1997. Rock Magnetism: Fundamentals and Frontiers, Vol. 51, First (9), Cambridge University Press, pp. 25–499. http://dx.doi.org/10.1063/1.882466,

Eugster, O., Weigel, A., Polnau, E., 1997. Ejection times of Martian meteorites. Geochim. Cosmochim. Acta 61 (13), 2749–2757. http://dx.doi.org/10.1016/S0016-7037(97)00115-4.

Fortin, D., Langley, S., 2005. Formation and occurrence of biogenic iron-rich minerals. Earth-Sci. Rev. 72 (1–2), 1–19. http://dx.doi.org/10.1016/j.earscirev.2005.03.002.

Fritz, J., Artemieva, N., Greshake, A., 2005a. Ejection of Martian meteorites. Meteorit. Planet. Sci. 40 (9–10), 1393–1411. http://dx.doi.org/10.1111/j.1945-5100.2005.tb00409.x, URL http://doi.wiley.com/10.1111/j.1945-5100.2005.tb00409.x.

Fritz, J., Greshake, A., Stoffler, D., 2005b. Micro-Raman spectroscopy of plagioclase and maskelynite in Martian meteorites: Evidence of progressive shock metamorphism. Antarctic Meteor. Res. 18, 96–116, URL https://ui.adsabs.harvard.edu/abs/2005AMR....18...96F/abstract.

Golden, D.C., Ming, D.W., Morris, R.V., Brearley, A.J., Lauer, H.V., Treiman, A.H., Zolensky, M.E., Schwandt, C.S., Lofgren, G.E., McKay, G.A., 2004. Evidence for exclusively inorganic formation of magnetite in Martian meteorite ALH84001. Am. Mineral. 89 (5–6), 681–695. http://dx.doi.org/10.2138/am-2004-5-602, URL http://pubs.geoscienceworld.org/msa/ammin/article-pdf/89/5-6/681/3617842/02_1413Golden.pdf.

Güldemeister, N., Wünnemann, K., Durr, N., Hiermaier, S., 2013. Propagation of impact-induced shock waves in porous sandstone using mesoscale modeling. Meteorit. Planet. Sci. 48 (1), 115–133. http://dx.doi.org/10.1111/j.1945-5100.2012.01430.x.

Hartmann, W.K., Neukum, G., 2001. Cratering chronology and the evolution of Mars. Space Sci. Rev. 96 (1–4), 165–194. http://dx.doi.org/10.1023/A:1011945222010.

Ismail, I.A., Murrell, S.A., 1990. The effect of confining pressure on stress-drop in compressive rock fracture. Tectonophysics 175 (1–3), 237–248. http://dx.doi.org/10.1016/0040-1951(90)90140-4.

Ivanov, B.A., Deniem, D., Neukum, G., 1997. Implementation of dynamic strength models into 2D hydrocodes: Applications for atmospheric breakup and impact cratering. Int. J. Impact Eng. 20 (1–5), 411–430. http://dx.doi.org/10.1016/s0734-743x(97)87511-2.

Jaret, S.J., Hemming, S.R., Rasbury, E.T., Thompson, L.M., Glotch, T.D., Ramezani, J., Spray, J.G., 2018. Context matters – Ar–Ar results from in and around the Manicouagan Impact Structure, Canada: Implications for martian meteorite chronology. Earth Planet. Sci. Lett. 501, 78–89. http://dx.doi.org/10.1016/j.epsl.2018.08.016.

Kirschvink, J.L., Maine, A.T., Vali, H., 1997. Paleomagnetic evidence of a low-temperature origin of carbonate in the martian meteorite ALH84001. Science 275 (5306), 1629–1633. http://dx.doi.org/10.1126/science.275.5306.1629, https://science.sciencemag.org/content/275/5306/1629, https://science.sciencemag.org/content/275/5306/1629.abstract.

Klemme, S., O'Neill, H.S.C., Schnelle, W., Gmelin, E., 2000. The heat capacity of MgCr2O4, FeCr2O4, and Cr2O3 at low temperatures and derived thermodynamic properties. Am. Mineral. 85, 1686–1693. http://dx.doi.org/10.2138/am-2000-11-1212.

Kring, D.A., Swindle, T.D., Gleason, J.D., Grier, J.A., 1998. Formation and relative ages of maskelynite and carbonate in ALH84001. Geochim. Cosmochim. Acta 62 (12), 2155–2166. http://dx.doi.org/10.1016/S0016-7037(98)00133-1.

Kurosawa, K., Genda, H., Azuma, S., Okazaki, K., 2021. The Role of Post-Shock Heating by Plastic Deformation During Impact Devolatilization of Calcite (CaCO3). In: Geophysical Research Letters, Vol. 48. (7), John Wiley & Sons, Ltd, http://dx.doi.org/10.1029/2020GL091130, e2020GL091130, https://agupubs.onlinelibrary.wiley.com/doi/full/10.1029/2020GL091130, https://agupubs.onlinelibrary.wiley.com/doi/abs/10.1029/2020GL091130, https://agupubs.onlinelibrary.wiley.com/doi/10.1029/2020GL091130.

Kurosawa, K., Okamoto, T., Genda, H., 2018. Hydrocode modeling of the spallation process during hypervelocity impacts: Implications for the ejection of Martian meteorites. Icarus 301, 219–234. http://dx.doi.org/10.1016/j.icarus.2017.09.015.

Lambert, P., Grieve, R.A., 1984. Shock experiments on maskelynite-bearing anorthosite. Earth Planet. Sci. Lett. 68 (1), 159–171. http://dx.doi.org/10.1016/0012-821X(84)90148-1.

Lapen, T.J., Righter, M., Brandon, A.D., Debaille, V., Beard, B.L., Shafer, J.T., Peslier, A.H., 2010. A younger age for ALH84001 and Its geochemical link to shergottite sources in mars. Science 328 (5976), 347–351. http://dx.doi.org/10.1126/science.1185395, URL http://science.sciencemag.org/.

Liu, Y., Xing, J., Li, Y., Tan, J., Sun, L., Yan, J., 2016. Mechanical properties and anisotropy of thermal conductivity of Fe3-xCrXO4 (x=0-3). J. Mater. Res. 31 (23), 3805–3813. http://dx.doi.org/10.1557/jmr.2016.425, URL https://www.cambridge.org/core/journals/journal-of-materials-research/article/abs/mechanical-properties-and-anisotropy-of-thermal-conductivity-of-fe3x-cr-x-o4-x-03/CF908F78703E7FB55245C40712A4E586.

Marsh, S.P., 1980. LASL Shock Hugoniot Data. University of California Press, p. 150, URL http://books.google.com/books?hl=en&lr=&id=-PCJtmM91JcC&oi=fnd&pg=PA1&dq=LASL+Shock+Hugoniot+Data&ots=T2G2fqQ7Vy&sig=pnut-H-jhuuZlsqS2snm_G6lnTc%5Cnhttp://large.stanford.edu/publications/coal/references/docs/shd.pdf.

McKay, D.S., Gibson, E.K., Thomas-Keprta, K.L., Vali, H., Romanek, C.S., Clemett, S.J., Chillier, X.D., Maechling, C.R., Zare, R.N., 1996. Search for past life on Mars: Possible relic biogenic activity in martian meteorite ALH84001. Science 273 (5277), 924–930. http://dx.doi.org/10.1126/science.273.5277.924.

Min, K., Reiners, P.W., 2007. High-temperature Mars-to-Earth transfer of meteorite ALH84001. Earth Planet. Sci. Lett. 260 (1–2), 72–85. http://dx.doi.org/10.1016/j.epsl.2007.05.019.

Mittlefehldt, D.W., 1994. ALH84001, a cumulate orthopyroxenite member of the martian meteorite clan. Meteoritics 29 (2), 214–221. http://dx.doi.org/10.1111/j.1945-5100.1994.tb00673.x, URL https://ui.adsabs.harvard.edu/abs/1994Metic..29..214M/abstract.

Moreau, J.G., Kohout, T., Wünnemann, K., Halodova, P., Haloda, J., 2019. Shock physics mesoscale modeling of shock stage 5 and 6 in ordinary and enstatite chondrites. Icarus 332, 50–65. http://dx.doi.org/10.1016/j.icarus.2019.06.004.

Murrell, S.A., Chakravarty, S., 1973. Some new rheological experiments on igneous rocks at temperatures up to 1120° c. Geophys. J. R. Astron. Soc. 34, 211–250. http://dx.doi.org/10.1111/j.1365-246X.1973.tb02394.x, URL https://academic.oup.com/gji/article/34/2/211/574514.

Nesterenko, V.F., 2001. Dynamics of Heterogeneous Materials. Springer, Berlin, http://dx.doi.org/10.1007/978-1-4757-3524-6.

O'Keefe, J.D., Ahrens, T.J., 1982. Impact mechanics of the cretaceous-tertiary extinction bolide. Nature 298 (5870), 123–127. http://dx.doi.org/10.1038/298123a0.

Pierazzo, E., Artemieva, N., Asphaug, E., Baldwin, E.C., Cazamias, J., Coker, R., Collins, G.S., Crawford, D.A., Davison, T., Elbeshausen, D., Holsapple, K.A., Housen, K.R., Korycansky, D.G., Wünnemann, K., 2008. Validation of numerical codes for impact and explosion cratering: Impacts on strengthless and metal targets. Meteorit. Planet. Sci. 43 (12), 1917–1938. http://dx.doi.org/10.1111/j.1945-5100.2008.tb00653.x, URL http://doi.wiley.com/10.1111/j.1945-5100.2008.tb00653.x.

Pierazzo, E., Kring, D.A., Jay Melosh, H., 1998. Hydrocode simulation of the Chicxulub impact event and the production of climatically active gases. J. Geophys. Res. E: Planets 103 (E12), 28607–28625. http://dx.doi.org/10.1029/98JE02496.

Potter, R.W., Collins, G.S., Kiefer, W.S., McGovern, P.J., Kring, D.A., 2012. Constraining the size of the South Pole-Aitken basin impact. Icarus 220 (2), 730–743. http://dx.doi.org/10.1016/j.icarus.2012.05.032.

Schmitz, B., Farley, K.A., Goderis, S., Heck, P.R., Bergström, S.M., Boschi, S., Claeys, P., Debaille, V., Dronov, A., van Ginneken, M., Harper, D.A., Iqbal, F., Friberg, J., Liao, S., Martin, E., Meier, M.M., Peucker-Ehrenbrink, B., Soens, B., Wieler, R., Terfelt, F., 2019. An extraterrestrial trigger for the mid-Ordovician ice age: Dust from the breakup of the L-chondrite parent body. Sci. Adv. 5 (9), 4184–4202. http://dx.doi.org/10.1126/sciadv.aax4184, URL https://www.science.org/doi/abs/10.1126/sciadv.aax4184.

Schulte, P., Alegret, L., Arenillas, I., Arz, J.A., Barton, P.J., Bown, P.R., Bralower, T.J., Christeson, G.L., Claeys, P., Cockell, C.S., Collins, G.S., Deutsch, A., Goldin, T.J., Goto, K., Grajales-Nishimura, J.M., Grieve, R.A., Gulick, S.P., Johnson, K.R., Kiessling, W., Koeberl, C., Kring, D.A., MacLeod, K.G., Matsui, T., Melosh, J., Montanari, A., Morgan, J.V., Neal, C.R., Nichols, D.J., Norris, R.D., Pierazzo, E., Ravizza, G., Rebolledo-Vieyra, M., Reimold, W.U., Robin, E., Salge, T., Speijer, R.P., Sweet, A.R., Urrutia-Fucugauchi, J., Vajda, V., Whalen, M.T., Willumsen, P.S., 2010. The chicxulub asteroid impact and mass extinction at the cretaceous-paleogene boundary. Science 327 (5970), 1214–1218. http://dx.doi.org/10.1126/science.1177265, URL https://www.science.org/doi/abs/10.1126/science.1177265.

Shimada, M., Cho, A., Yukutake, H., 1983. Fracture strength of dry silicate rocks at high confining pressures and activity of acoustic emission. Tectonophysics 96 (1–2), 159–172. http://dx.doi.org/10.1016/0040-1951(83)90248-2.

Shuster, D.L., Weiss, B.P., 2005. Planetary science: Martian surface paleotemperatures from thermochronology of meteorites. Science 309 (5734), 594–597. http://dx.doi.org/10.1126/science.1113077, URL www.sciencemag.org/cgi/content/full/309/5734/591/.

Steele, A., Fries, M.D., Amundsen, H.E., Mysen, B.O., Fogel, M.L., Schweizer, M., Boctor, N.Z., 2007. Comprehensive imaging and Raman spectroscopy of carbonate globules from Martian meteorite ALH 84001 and a terrestrial analogue from Svalbard. Meteorit. Planet. Sci. 42 (9), 1549–1566. http://dx.doi.org/10.1111/j.1945-5100.2007.tb00590.x.

Steele, S.C., Fu, R.R., Volk, M.W.R., North, T.L., Brenner, A.R., Collins, G.S., Davison, T.M., Muxworthy, A.R., 2022. Paleomagnetic evidence for a long-lived reversing Martian dynamo at 3.9 Ga. LPSC LIII Abstract #1764, URL https://www.hou.usra.edu/meetings/lpsc2022/pdf/1764.pdf.

Stöffler, D., Keil, K., Edward R.D, S., 1991. Shock metamorphism of ordinary chondrites. Geochim. Cosmochim. Acta 55 (12), 3845–3867. http://dx.doi.org/10.1016/0016-7037(91)90078-J.

Thomas-Keprta, K.L., Bazylinski, D.A., Kirschvink, J.L., Clemett, S.J., McKay, D.S., Wentworth, S.J., Vali, H., Gibson, E.K., Romanek, C.S., 2000. Elongated prismatic magnetite crystals in ALH84001 carbonate globules: Potential Martian magnetofossils. Geochim. Cosmochim. Acta 64 (23), 4049–4081. http://dx.doi.org/10.1016/S0016-7037(00)00481-6.

Thomas-Keprta, K.L., Clemett, S.J., Bazylinski, D.A., Kirschvink, J.L., McKay, D.S., Wentworth, S.J., Vali, H., Gibson, E.K., McKay, M.F., Romanek, C.S., 2001. Truncated hexa-octahedral magnetite crystals in ALH84001: Presumptive biosignatures. Proc. Natl. Acad. Sci. USA 98 (5), 2164–2169. http://dx.doi.org/10.1073/pnas.051500898, URL www.pnas.orgcgidoi10.1073pnas.051500898.

Tillotson, J.H., 1962. Metallic equations of state for hypervelocity impacts. Report No. GA-3216, General At., San Diego, CA 43, https://ui.adsabs.harvard.edu/abs/1962geat.rept.3216T/abstract, http://oai.dtic.mil/oai/oai?verb=getRecord&metadataPrefix=html&identifier=AD0486711.

Treiman, A.H., 1995. A petrographic history of martian meteorite ALH84001: Two shocks and an ancient age. Meteoritics 30 (3), 294–302. http://dx.doi.org/10.1111/j.1945-5100.1995.tb01127.x, https://onlinelibrary.wiley.com/doi/full/10.1111/j.1945-5100.1995.tb01127.x, https://onlinelibrary.wiley.com/doi/abs/10.1111/j.1945-5100.1995.tb01127.x, https://onlinelibrary.wiley.com/doi/10.1111/j.1945-5100.1995.tb01127.x.

Treiman, A.H., 1998. The history of Allan Hills 84001 revised: multiple shock events. Meteorit. Planet. Sci. 33 (4), 753–764. http://dx.doi.org/10.1111/j.1945-5100.1998.tb01681.x, URL http://doi.wiley.com/10.1111/j.1945-5100.1998.tb01681.x.

Treiman, A.H., 2021. Uninhabitable and Potentially Habitable Environments on Mars: Evidence from Meteorite ALH 84001. Astrobiology 21 (8), 940–953. http://dx.doi.org/10.1089/ast.2020.2306, URL https://www.liebertpub.com/doi/abs/10.1089/ast.2020.2306.

Treiman, A.H., Essene, E.J., 2011. Chemical composition of magnetite in Martian meteorite ALH 84001: Revised appraisal from thermochemistry of phases in Fe-Mg-C-O. Geochim. Cosmochim. Acta 75 (18), 5324–5335. http://dx.doi.org/10.1016/j.gca.2011.06.038.

Turner, G., Knott, S.F., Ash, R.D., Gilmour, J.D., 1997. Ar-Ar chronology of the Martian meteorite ALH84001: Evidence for the timing of the early bombardment of Mars. Geochim. Cosmochim. Acta 61 (18), 3835–3850. http://dx.doi.org/10.1016/S0016-7037(97)00285-8, URL https://pubmed.ncbi.nlm.nih.gov/11541217/.

van Thiel, M., Shaner, J., Salinas, E., 1977. Compendium of Shock Wave Data. Technical Report, Livermore, pp. 396–398, URL https://inis.iaea.org/search/search.aspx?orig_q=RN:9407663.

Weiss, B.P., Berdahl, J.S., Elkins-Tanton, L., Stanley, S., Lima, E.A., Carporzen, L., 2008a. Magnetism on the angrite parent body and the early differentiation of planetesimals. Science 322 (5902), 713–716. http://dx.doi.org/10.1126/science.1162459.

Weiss, B.P., Fong, L.E., Vali, H., Lima, E.A., Baudenbacher, F.J., 2008b. Paleointensity of the ancient Martian magnetic field. Geophys. Res. Lett. 35 (23), 23207. http://dx.doi.org/10.1029/2008GL035585, https://agupubs.onlinelibrary.wiley.com/doi/full/10.1029/2008GL035585, https://agupubs.onlinelibrary.wiley.com/doi/abs/10.1029/2008GL035585, https://agupubs.onlinelibrary.wiley.com/doi/10.1029/2008GL035585.

Weiss, B.P., Kim, S.S., Kirschvink, J.L., Kopp, R.E., Sankaran, M., Kobayashi, A., Komeili, A., 2004. Magnetic tests magnetosome chains in Martian meteorite ALH84001. Proc. Natl. Acad. Sci. USA 101 (22), 8281–8284. http://dx.doi.org/10.1073/pnas.0402292101, URL https://www.pnas.org/doi/abs/10.1073/pnas.0402292101.

Weiss, B.P., Kirschvink, J.L., Baudenbacher, F.J., Vali, H., Peters, N.T., Macdonald, F.A., Wikswo, J.P., 2000. A low temperature transfer of ALH84001 from Mars to Earth. Science 290 (5492), 791–795. http://dx.doi.org/10.1126/science.290.5492.791, URL www.sciencemag.orghttp://science.sciencemag.org/.

Weiss, B.P., Vali, H., Baudenbacher, F.J., Kirschvink, J.L., Stewart, S.T., Shuster, D.L., 2002. Records of an ancient Martian magnetic field in ALH84001. Earth Planet. Sci. Lett. 201 (3–4), 449–463. http://dx.doi.org/10.1016/S0012-821X(02)00728-8, URL www.elsevier.com/locate/epsl.

Wünnemann, K., Collins, G.S., Melosh, H.J., 2006. A strain-based porosity model for use in hydrocode simulations of impacts and implications for transient crater growth in porous targets. Icarus 180 (2), 514–527. http://dx.doi.org/10.1016/j.icarus.2005.10.013, https://www.sciencedirect.com/science/article/abs/pii/S0019103505004124?via%3Dihub, https://www.sciencedirect.com/science/article/pii/S0019103505004124?via%3Dihub.